Slowly rotating ultra-compact Schwarzschild star in the gravastar limit

Philip Beltracchi and Camilo Posada^{1,2}

¹Research Centre for Theoretical Physics and Astrophysics, Institute of Physics,
 Silesian University in Opava, Bezručovo nám. 13, CZ-746 01 Opava, Czech Republic
 ²Programa de Matemática, Fundación Universitaria Konrad Lorenz, 110231 Bogotá,
 Colombia

E-mail: phipbel@aol.com and camilo.posada@physics.slu.cz

Abstract.

We reconsider the problem of a slowly rotating homogeneous star, or Schwarzschild star, when its compactness goes beyond the Buchdahl bound and approaches the gravastar limit $R \to 2M$. We compute surface and integral properties of such configuration by integrating the Hartle-Thorne structure equations for slowly rotating relativistic masses, at second order in angular velocity. In the gravastar limit, we show that the metric of a slowly rotating Schwarzschild star agrees with the Kerr metric, thus, within this approximation, it is not possible to tell a gravastar from a Kerr black hole by any observations from the spacetime exterior to the horizon.

Keywords: interior solution, gravastars, ultra-compact stars, rotation, Hartle-Thorne metric.

1. Introduction

It has been known for a long time, that a star whose mass exceeds some critical value, and which is contained in a sufficiently small region, will develop trapped surfaces. Under certain conditions, this will subsequently lead to gravitational collapse to a singular state called a 'black hole' (BH) [1]. These results are known as the singularity theorems [2, 3]. The BH has been the source of plethora of investigations in the last 60 years (see e.g [4, 5, 6], and references therein), reaching recently a peak with the LIGO/Virgo detection of gravitational waves signals of the merger of two BHs [7, 8], and the outstanding images of M87 [9] and Sagittarius A* [10], provided by the Event Horizon Telescope collaboration.

One of the key features of mathematical BHs is the so-called event horizon, which is a marginally trapped surface where no information whatsoever can escape [1]. This event horizon, has been the root of severe issues in BH physics, like the 'BH information paradox' [11], which despite many proposals (see e.g. [12] and references therein), remains as one of the biggest challenges of the BH paradigm. Although the exterior geometry of BHs is free of pathologies, and it has been thoroughly studied [13], the

interior is not; for instance, standard BHs hold curvature singularities in their interior which breaks the classical concepts of space and time as well as the known laws of physics [11]. Curvature singularities are a feature of the interior for the standard Schwarzschild, Reissner-Nordström, Kerr, and Kerr-Newman models of BHs [13]. Additionally, Kerr BHs predict the existence of acausal closed timelike geodesics in their interior [1].

Certain models of non-singular BHs, or BH mimickers, have been introduced in the literature, as a way out to the BH paradoxes [14]. These objects avoid the appearance of singularities by violating one or more of the assumptions of the singularity theorems. One of the most popular models is the gravastar proposed by Mazur and Mottola [15, 16]. The gravastar is characterized by an interior de Sitter region with a positive (and constant) energy density ϵ , and a negative pressure $p = -\epsilon$, which is matched to the exterior Schwarzschild spacetime by a timelike thin-shell boundary of thickness $l \sim (L_{\rm Pl} r_M)^{1/2}$, where $L_{\rm Pl}$ is the Planck length, and $r_M \sim r_{\rm H}$ is the boundary of the mutual de Sitter and Schwarzschild horizons. This collapsed cold dark object, has no event horizon, a regular interior, and a globally defined Killing time. Moreover, in contrast with classical BHs, the gravastar does not suffer from huge entropies and information paradox.

Various generalizations of the gravastar model have been under scrutiny during the last 20 years [17, 18, 19, 20, 21, 22, 23, 24, 25, 26, 27, 28, 29, 30, 31, 32, 33]. Gravitational wave signatures and non-radial oscillations of thin-shell gravastars were studied by [22, 23, 24, 25]. Some models of rotating gravastars have been proposed by a number of authors [26, 27, 28, 29, 30, 31, 32]. In this context, the ergoregion instability of rotating gravastars, which affects compact objects rotating rapidly, was investigated by [26, 27]. For instance, [26] found that some stable gravastars can be constructed with $J/M^2 \sim 1$, with J being the angular momentum and M is the total mass; thus not all of the astrophysical objects rotating with $J/M^2 < \sim 1$ are to be considered BHs.

The gravastar as pictured originally in [15, 16], has been reexamined by [34], after the realization that an infinitesimally thin-shell gravastar emerges naturally from the Schwarzschild's interior solution with constant density [35], or 'Schwarzschild star'. It is well-known that the central pressure of the Schwarzschild star diverges when its radius reaches the Buchdahl bound $R_{\rm B} \equiv (9/4)M$. Thus, the constant density solution saturates the Buchdahl theorem [36], which establishes that the radius of a star must satisfy the inequality $R \geq (9/4)M$, in order to be in hydrostatic equilibrium, regardless of the equation of state, if the pressure is positive and isotropic.

By contracting adiabatically the Schwarzschild star, beyond the Buchdahl bound, [34] showed that the central pressure divergence moves outward from the origin to a surface $R_0 = 3R\sqrt{1 - (8/9)(R/R_S)}$ and a negative pressure region opens up behind it. In the limit when the radius of the star approaches the Schwarzschild radius $R_S \equiv 2M$, the Schwarzschild star produces a $p = -\epsilon$ interior, which is matched to the exterior Schwarzschild spacetime by an infinitesimally thin (null) boundary layer of anisotropic stresses localized at R_S . Thus, in this limit, the Schwarzschild star becomes essentially the gravastar.

The Schwarzschild star has been shown to be stable against radial oscillations [37]. Axial non-spherical perturbations of ultracompact Schwarzschild stars were considered by [38]. These authors showed that the observable quasi-normal modes can be as close as one wishes to the Schwarzschild limit, making it a very good BH mimicker. Moreover, the decaying time-domain profile shows that the ultracompact Schwarzschild star is stable against axial oscillations (although no echoes were found). An exact solution for dynamical collapse of a modified anisotropic Schwarzschild star was found by [39]. Chirenti et. al. [40] determined the tidal Love number k_2 of 'sub-Buchdahl' Schwarzschild stars, and they found that it is strongly dependent on the compactness M/R; moreover, in the Schwarzschild limit, $k_2 \to 0$, thus a gravastar cannot be distinguished from a BH by its tidal deformability.

A first extension of the ultracompact Schwarzschild star to slow rotation was proposed in [41] by employing the Hartle-Thorne (HT) [42, 43] perturbative approach for computing the properties of slowly rotating relativistic stars to second order in the angular velocity, together with the methods introduced by Chandrasekhar and Miller [44] for slowly rotating Schwarzschild stars, below the Buchdahl limit. However, as it was pointed out by [45], the results reported by [41], beyond the Buchdahl limit, were marred after an incorrect assumption in a coordinate transformation. While it is possible to solve Hartle's equations for dark energy analytically [28, 29, 45, 46], the $R \to 2M$ limit of numerically computed slowly rotating Schwarzschild stars can provide a valuable point of comparison to these analytic results, especially to those of [45] which used a null boundary and the same interior time scaling of the Schwarzschild derived gravastar from [34].

In this paper we reconsider the problem studied in [41] of a slowly rotating Schwarzschild star when its compactness goes beyond the Buchdahl bound and approaches the gravastar limit $R \to R_{\rm S}$. We follow the formulation of [44], where the HT structure equations were integrated for a Schwarzschild star up to the Buchdahl limit. Our approach will complete, and improve, the one presented by [41] in various directions. First, we apply boundary conditions of the HT equations at R_0 , rather than the origin [47], which allowed us to compute surface and integral properties (i.e., physical properties of the object like moment of inertia, change in mass, etc., evaluated at the surface) in the regime $R_{\rm S} < R < (9/8)R_{\rm S}$. Second, we discuss the inward extension of the solution to the perturbation equation, inside the infinite surface pressure surface R_0 . We found that in the gravastar limit, the perturbation functions and quantities like the moment of inertia, and mass quadrupole moment, approach the corresponding Kerr BH values. Thus, our results indicate that the exterior spacetime of a slowly rotating gravastar cannot be differentiated to that of a slowly rotating Kerr BH.

The paper is organized as follows: in section 2 we review the Schwarzschild interior solution for incompressible fluids, or Schwarzschild star, and its approach to the gravastar limit. In section 3 we summarize the general Hartle-Thorne framework for slowly rotating relativistic stars. In section 4 we apply the HT approximation to the Schwarzschild stars. In section 5 we present our methods and results of surface

and integral properties, where in section 5.1 we discuss our results for frame dragging and moment of inertia. Results related to the monopole perturbations, such as the properties of m_0 , h_0 , p_0^* , ξ_0 , and the change in mass δM are presented in section 5.2. The properties of the quadrupole perturbations m_2 , h_2 , k_2 , and p_2^* , together with the external parameters ξ_2 , mass quadrupole moment Q, and ellipticity ϵ , as well as the I-Q relation, are presented in section 5.3. Section 6 contains our final conclusions. We use geometrized units (G = c = 1), unless stated otherwise, and we adopt the metric signature (-, +, +, +).

There are three appendices. The first contains a series solution to the 'dragging' equation, where we argue on the choice of the branch ϖ_1 . In Appendix B we provide a consistency check between the (r, R) and (κ, x) coordinates. Finally, in Appendix C, we determine the surface gravity and angular momentum parameters of the slowly rotating Schwarzschild stars.

2. Spherically symmetric Schwarzschild star in the gravastar limit

2.1. Non-rotating configuration in hydrostatic equilibrium

The nonrotating configuration is described by a metric in the standard spherically symmetric form

$$ds^{2} = -e^{2\nu(r)}dt^{2} + e^{2\lambda(r)}dr^{2} + r^{2}(d\theta^{2} + \sin^{2}\theta d\phi^{2}), \tag{2.1}$$

where ν and λ are only functions of r. We assume a perfect fluid with an isobaric equation of state, i.e., $\epsilon = \epsilon(p)$, which connects the pressure p with the mass-energy density ϵ . For a given value of the central energy density ϵ_c , the nonrotating configuration is determined by solving the Tolman-Oppenheimer-Volkoff (TOV) equation of hydrostatic equilibrium for the pressure p(r), and the mass enclosed by a given radius m(r)

$$\frac{dp}{dr} = -(\epsilon + p)\frac{m(r) + 4\pi pr^3}{r[r - 2m(r)]},$$
(2.2)

$$\frac{dm(r)}{dr} = 4\pi\epsilon(r)r^2. \tag{2.3}$$

The mass function m(r) is connected with the metric component g_{rr} by the relation

$$e^{-2\lambda(r)} \equiv 1 - \frac{2m(r)}{r},\tag{2.4}$$

and the time-component metric g_{tt} can be obtained as

$$\frac{d\nu}{dr} = -\frac{1}{(\epsilon + p)} \left(\frac{dp}{dr}\right). \tag{2.5}$$

In the exterior vacuum space-time $\epsilon = p = 0$, thus the geometry is described by the Schwarzschild metric

$$e^{2\nu(r)} = e^{-2\lambda(r)} = 1 - \frac{2M}{r}, \quad r > R,$$
 (2.6)

where R is the radius and m(R) = M is the total gravitational mass of the configuration. The interior and exterior spacetimes are matched across the boundary $\Sigma = R$, such that

$$[\lambda] = 0, \quad [\nu] = 0, \quad [\nu'] = 0,$$
 (2.7)

where [f] indicates the difference between the value of f in the vacuum exterior and its value in the interior, evaluated at Σ , i.e., $[f] = f^+|_{\Sigma} - f^-|_{\Sigma}$, and the prime denotes derivative with respect to the radial coordinate $r \ddagger$.

2.2. Schwarzschild's interior solution in the gravastar limit

If we model the star as an incompressible and isotropic fluid with

$$\epsilon = \frac{3M}{4\pi R^3} = \frac{3H^2}{8\pi} = \text{constant},\tag{2.8}$$

where $H^2 = R_S/R^3$, by solving equations (2.2)-(2.5) we obtain the well-known Schwarzschild's interior solution with constant density [35] (a.k.a. Schwarzschild star)

$$e^{2\nu(r)} = \frac{1}{4} \left[3\sqrt{1 - H^2 R^2} - \sqrt{1 - H^2 r^2} \right]^2, \tag{2.9}$$

$$e^{-2\lambda(r)} = 1 - H^2 r^2, (2.10)$$

$$p(r) = \epsilon \left[\frac{\sqrt{1 - H^2 r^2} - \sqrt{1 - H^2 R^2}}{3\sqrt{1 - H^2 R^2} - \sqrt{1 - H^2 r^2}} \right]. \tag{2.11}$$

At the boundary of the configuration r = R, this solution must match with the exterior solution (2.6), and the pressure must vanish p(R) = 0. The continuity of g_{tt} guarantees that an observer crossing the boundary will not notice any discontinuity of time measurements.

From (2.11) we note that the central pressure blows up when the stellar radius reaches the Buchdahl limit $R_{\rm B} \equiv (9/8)R_{\rm S}$. As it was shown by Buchdahl [36], under certain assumptions, this limit is actually independent of the equation of state describing the fluid. Thus, in order to be in hydrostatic equilibrium the radius of a star must satisfy the inequality $R \geq (9/8)R_{\rm S}$. In connection with this, we observe that (2.11) is regular except at some radius R_0 where the denominator

$$D(r) \equiv 3\sqrt{1 - H^2R^2} - \sqrt{1 - H^2r^2},\tag{2.12}$$

vanishes in the range 0 < r < R. Remarkably, it can be seen from (2.9) and (2.11) that the pressure goes to infinity at the same point where $e^{2\nu} = 0$. This singular radius can be found directly from (2.12) as

$$R_0 = 3R\sqrt{1 - \frac{8}{9}\frac{R}{R_S}},\tag{2.13}$$

which is imaginary for R above the Buchdahl limit. As $R \to (9/8)R_S$, from above, (2.13) shows that R_0 approaches the real axis at $R_0 = 0$ and a divergence of the pressure

‡ We use the opposite convention from [48], who uses +(-) to denote quantities in the interior (exterior).

appears as $e^{2\nu} \to 0$. Note that when $R = R_B$, $R_0 = 0$, thus the pole appears first at the origin. Mazur and Mottola [34] studied further the region beyond the Buchdahl limit, i.e. $R_S < R < (9/8)R_S$, and they found that R_0 moves outwards from the origin to finite values $0 < R_0 < R$ (see figure 1 in [41]). Thus, there emerges naturally a new region $0 \le r < R_0$, where D(r) < 0, and in consequence p(r) < 0, while $e^{2\nu} > 0$. As the adiabatic and quasi-stationary contraction continues from above, i.e., $R \to R_S^+$, $R_0 \to R_S^-$ from below thus the region $0 < r < R_0$ with negative pressure keeps growing while the region with positive pressure $R_0 < r < R$ squeezes (see figure 3 in [41]). In the limit when $R = R_0 = R_S$, the Schwarzschild's interior solution (2.9), (2.10) and (2.11) becomes

$$e^{2\nu(r)} = \frac{1}{4} \left(1 - \frac{r^2}{R_S^2} \right), \quad e^{2\lambda(r)} = \left(1 - \frac{r^2}{R_S^2} \right)^{-1},$$
 (2.14)

$$p = -\epsilon, \tag{2.15}$$

which is essentially the gravastar proposed in [34], parametrized by the total mass M. The exterior region $r > R_{\rm S}$ remains the vacuum spherically symmetric Schwarzschild geometry (2.6), with an infinitesimal thin shell discontinuity at the surface $R_{\rm S}$ where there is a jump in pressure and the zeroes $e^{2\nu} = e^{2\lambda} = 0$ of the interior de Sitter and exterior Schwarzschild spacetimes match.

The divergence in pressure at R_0 can be integrated through the Komar formula, if one assumes that $p_{\perp} \neq p$, thus relaxing the isotropic fluid condition. Beyond the Buchdahl bound, $R/R_{\rm S} < 9/8$, the relation for pressure is [34]

$$8\pi\sqrt{\frac{f}{h}}r^2(p_{\perp} - p) = \frac{8\pi\epsilon}{3}R_0^3\delta(r - R_0),\tag{2.16}$$

indicating the presence of a δ -distributional anisotropic stress tensor at $r = R_0$, which produces a surface tension

$$\tau_s = \frac{[\kappa]}{8\pi} = \frac{1}{16\pi M},\tag{2.17}$$

that is proportional to the difference in surface gravities

$$[\kappa] \equiv \kappa_+ - \kappa_- = \frac{R_{\rm S} R_0}{R^3}.\tag{2.18}$$

In contrast to a BH, (2.17) corresponds to a physical surface tension (localized in an infinitesimal thin shell at $r = R_{\rm S}$) provided by a positive transverse pressure as determined by the Komar formula. The boundary $r = R_{\rm S}$ is a null hypersurface, but it is not an event horizon, thus there is no 'information paradox'. Moreover, there are no trapped surfaces in the region $r < R_{\rm S}$, and it has a regular interior free of singularities. Furthermore, the gravastar is a cold condensate state with low entropy in contrast to BHs which possesses huge entropies as predicted by the Bekenstein-Hawking formula, far in excess of the stellar progenitors [15].

3. Hartle-Thorne formalism for rotational metric deformations

Once the equilibrium configuration is set into slow rotation, the interior distribution and the spacetime geometry change. The appropriate line element for this situation is the so-called Hartle-Thorne metric [42, 43]

$$ds^{2} = -e^{2\nu} \left[1 + 2h_{0}(r) + 2h_{2}(r)P_{2}(\cos\theta) \right] dt^{2}$$

$$+ e^{2\lambda} \left\{ 1 + \frac{e^{2\lambda}}{r} \left[2m_{0}(r) + 2m_{2}(r)P_{2}(\cos\theta) \right] \right\} dr^{2}$$

$$+ r^{2} \left[1 + 2k_{2}(r)P_{2}(\cos\theta) \right] \left[d\theta^{2} + \sin^{2}\theta (d\phi - \omega dt)^{2} \right],$$
(3.1)

where $P_2(\cos \theta)$ is the Legendre polynomial of order 2; $(h_0, h_2, m_0, m_2, k_2)$ are quantities of order Ω^2 ; and $\omega(r)$ (of order Ω) is the 'dragging' function corresponding to the angular velocity of the local inertial frame, relative to a distant observer. The angular velocity of the star, as measured by distant observers, is indicated by Ω . In the nonrotating case, the metric (3.1) reduces to (2.1).

3.1. Moment of inertia and dragging of inertial frames

We assume the fluid, inside the configuration, rotating uniformly with four-velocity u^{μ} given by

$$u^{t} = (-g_{tt} - 2\Omega g_{t\phi} - g_{\phi\phi}\Omega^{2})^{-1/2}$$

$$= e^{-\nu} \left[1 + \frac{1}{2}r^{2}\sin^{2}\theta(\Omega - \omega)^{2}e^{-2\nu} - h_{0} - h_{2}P_{2} \right],$$

$$u^{\phi} = \Omega u^{t}, \quad u^{r} = u^{\theta} = 0.$$

It is conventional to introduce the quantity

$$\varpi \equiv \Omega - \omega, \tag{3.2}$$

that corresponds to the angular velocity of the fluid relative to the local inertial frame. This quantity determines the centrifugal force and, at first order in Ω , satisfies the following equation [42, 43]

$$\frac{d}{dr}\left[r^4j(r)\frac{d\varpi}{dr}\right] + 4r^3\frac{dj}{dr}\varpi = 0,$$
(3.3)

where

$$j(r) \equiv e^{-(\lambda+\nu)}. (3.4)$$

In the region r > R, $\epsilon = p = 0$ and the spacetime geometry is described by (2.6); thus, j(r) = 1 and (3.3) can be easily integrated to give

$$\varpi(r)^{+} = \Omega - \frac{2J}{r^{3}},\tag{3.5}$$

where J is an integration constant associated with the angular momentum of the star [42]. For nonsingular well behaved solutions, it can be proved, using series arguments, that the appropriate boundary conditions for (3.3) are, $\varpi(0) = \varpi_c = \text{const.}$, and

 $(d\varpi/dr)|_{r=0}=0$, after which it is integrated outward. Regularity demands that, at the surface, the interior and exterior solutions, together with their derivatives, must match, i.e., $[\varpi]=[\varpi']=0$. Thus, one integrates numerically (3.3) and obtains the surface value $\varpi(R)$, then, and only then, one can determine the angular momentum J and the angular velocity Ω as

$$J = \frac{1}{6}R^4 \left(\frac{d\varpi}{dr}\right)_{r=R}, \quad \Omega = \varpi(R) + \frac{2J}{R^3}.$$
 (3.6)

Once the angular momentum and angular velocity are determined, the relativistic moment of inertia can be obtained by the relation $I = J/\Omega$.

3.2. Spherical deformations of the star: l = 0 sector

In the interior of the star, the pressure can be expanded as

$$p_{\text{tot}}(r) = p + (\epsilon + p) \left[p_0^* + p_2^* P_2(\cos \theta) \right],$$
 (3.7)

where p_{tot} is the pressure in the rotating system, ϵ and p are the density and pressure in the background system, and p_0^* and p_2^* are functions of r proportional to Ω^2 , associated to the perturbations in the pressure.

The equations for the l = 0 sector, for the mass perturbation factor m_0 , and pressure perturbation factor p_0^* read [43, 44]

$$\frac{dm_0}{dr} = 4\pi r^2 (\epsilon + p) \left(\frac{d\epsilon}{dp}\right) p_0^* + \frac{1}{12} r^4 j^2 \left(\frac{d\varpi}{dr}\right)^2 - \frac{1}{3} r^3 \varpi^2 \frac{dj^2}{dr},\tag{3.8}$$

$$\frac{dp_0^*}{dr} = -\frac{1 + 8\pi pr^2}{(r - 2m)^2} m_0 - \frac{4\pi (\epsilon + p)r^2}{r - 2m} p_0^* + \frac{1}{12} \frac{r^4 j^2}{(r - 2m)} \left(\frac{d\omega}{dr}\right)^2 + \frac{1}{3} \frac{d}{dr} \left(\frac{r^3 j^2 \omega^2}{r - 2m}\right).$$
(3.9)

These equations are integrated outward with the boundary conditions $m_0 = p_0^* = 0$ at the origin, with $m_0(0) = 0$ indicating the lack of a point mass term to the perturbations, and $p_0^*(0) = 0$ being conventional in the formalism [42, 43]. The function h_0 in the interior of the configuration can be determined from the equation of hydrostatic equilibrium as follows [43, 44]

$$h_0^- = -p_0^* + \frac{1}{3}r^2 e^{-2\nu} \varpi^2 + h_c, \tag{3.10}$$

where h_c is a constant of integration. In the exterior of the star, where $\epsilon = p = 0$, (3.8) and (3.9) are integrated explicitly giving

$$m_0^+(r) = \delta M - \frac{J^2}{r^3},$$
 (3.11)

$$h_0^+(r) = -\frac{\delta M}{r - 2M} + \frac{J^2}{r^3(r - 2M)},$$
 (3.12)

where δM is a constant of integration associated with the change in mass induced by

the rotation. The constants h_c and δM can be found by the continuity of the solutions at the surface Σ , i.e., $[h_0] = [m_0] = 0$.

As it was pointed out by [49], expression (3.11) for δM is not the most general one. By reconsidering the matching problem in Hartle's framework, by employing the perturbed matching theory at second order developed by [50], [49] showed that the perturbative functions are continuous across the surface Σ , except for the function $m_0(r)$ in the l=0 sector. The discontinuity in $m_0(r)$ turns out to be proportional to the energy density at Σ , thus contributing an additional term to (3.11) in the form

$$\delta M_{\text{mod}} = m_0(R) + \frac{J^2}{R^3} + 8\pi R^3 \left(\frac{R}{2M} - 1\right) \epsilon(R) p_0^*, \tag{3.13}$$

such that the total mass of the star is $M(R) + \delta M_{\text{mod}}$. Note that for configurations with a vanishing surface energy density, as is the case for most of the equations of state for realistic NSs, this additional term vanishes; thus the original expression (3.11) remains valid. However, for configurations with a discontinuity in ϵ at the surface, e.g. constant density stars or strange stars, this additional term provides a significant contribution to the change in mass [48].

3.3. Quadrupole deformations of the star: l=2 sector

The quadrupole deformations of the star are determined by the l=2 perturbation equations given by [43, 44]

$$\frac{dv_{2}}{dr} = -2\left(\frac{d\nu}{dr}\right)h_{2} + \left(\frac{1}{r} + \frac{d\nu}{dr}\right)\left[\frac{1}{6}r^{4}j^{2}\left(\frac{d\varpi}{dr}\right)^{2} - \frac{1}{3}r^{3}\varpi^{2}\frac{dj^{2}}{dr}\right], \quad (3.14)$$

$$\frac{dh_{2}}{dr} = -\frac{2v_{2}}{r\left[r - 2m(r)\right]}\left(\frac{d\nu}{dr}\right)^{-1} + \left\{-2\frac{d\nu}{dr} + \frac{r}{2\left[r - 2m(r)\right]}\left(\frac{d\nu}{dr}\right)^{-1}\left[8\pi(\epsilon + p) - \frac{4m(r)}{r^{3}}\right]\right\}h_{2}$$

$$+ \frac{1}{6}\left[r\left(\frac{d\nu}{dr}\right) - \frac{1}{2\left[r - 2m(r)\right]}\left(\frac{d\nu}{dr}\right)^{-1}\right]r^{3}j^{2}\left(\frac{d\varpi}{dr}\right)^{2}$$

$$- \frac{1}{3}\left[r\left(\frac{d\nu}{dr}\right) + \frac{1}{2\left[r - 2m(r)\right]}\left(\frac{d\nu}{dr}\right)^{-1}\right]r^{2}\frac{dj^{2}}{dr}\varpi^{2}, \quad (3.15)$$

where

$$k_2 = v_2 - h_2. (3.16)$$

In the exterior where $\epsilon=p=0$, equations (3.14) and (3.15) can be integrated analytically to give

$$h_2^+(r) = \frac{J^2}{Mr^3} \left(1 + \frac{M}{r} \right) + KQ_2^2(\zeta), \tag{3.17}$$

$$v_2^+(r) = -\frac{J^2}{r^4} + K \frac{2M}{[r(r-2M)]^{1/2}} Q_2^{1}(\zeta), \tag{3.18}$$

where K is a constant of integration and Q_n^m are the associated Legendre functions of the second kind with argument $\zeta \equiv (r/M) - 1$. The condition of regularity of the solutions at the surface Σ requires $[h_2] = [v_2] = 0$. The constant K appearing in (3.17) and (3.18), is connected with the quadrupole mass moment of the star, as measured at infinity, via the relation [43]

$$Q = \frac{J^2}{M} + \frac{8}{5}KM^3. (3.19)$$

To find the constant K, the functions h_2 and v_2 must be computed for the interior of the star, and then matched at the surface Σ with the exterior solutions (3.17) and (3.18).

The perturbations for mass and pressure m_2 and p_2^* , which determine the rotational deformations of the star, can be determined using the following relations [43, 44]

$$m_2 = (r - 2m) \left[-h_2(r) - \frac{1}{3}r^3 \left(\frac{dj^2}{dr} \right) \varpi^2 + \frac{1}{6}r^4 j^2 \left(\frac{d\varpi}{dr} \right)^2 \right],$$
 (3.20)

$$p_2^* = -h_{2(r)} - \frac{1}{3}r^2 e^{-2\nu} \varpi^2.$$
(3.21)

The rotational perturbations will displace the nonrotating surface to the radius [42, 43, 44]

$$r^*(p) = r + \xi_0(r) + \xi_2(r)P_2(\cos\theta), \tag{3.22}$$

where r is the radius of the nonrotating configuration with pressure p; ξ_0 and ξ_2 are perturbation functions which satisfy the following relations [43, 44]

$$p_0^* = -\left[\frac{dp/dr}{(\epsilon+p)}\right]_0 \xi_0(r), \quad p_2^* = -\left[\frac{dp/dr}{(\epsilon+p)}\right]_0 \xi_2(r),$$
 (3.23)

where the terms in square brackets are evaluated in the nonrotating configuration. Using (2.5) we can rewrite (3.23) in the following form

$$\xi_0(r) = \left(\frac{d\nu}{dr}\right)^{-1} p_0^*, \quad \xi_2(r) = \left(\frac{d\nu}{dr}\right)^{-1} p_2^*.$$
 (3.24)

The ellipticity of the isobaric surfaces is determined by [44]

$$\varepsilon(r) = -\frac{3}{2r} \left[\xi_2(r) + r \left(v_2 - h_2 \right) \right]. \tag{3.25}$$

In the following sections, we will apply the HT approximation to the Schwarzschild star, and study its approach to the gravastar limit.

4. Hartle-Thorne framework for slowly rotating Schwarzschild stars

Here we summarize the HT structure equations for slowly rotating Schwarzschild stars, as described by the interior Schwarzschild's solution with uniform density, which we discussed in section 2.2. Following the conventions of [44], equations (2.9)-(2.11) can be rewritten as

$$e^{2\lambda} = \frac{1}{y^2}, \quad e^{2\nu} = \frac{1}{4}(3y_1 - y)^2,$$
 (4.1)

Slowly rotating ultra-compact Schwarzschild star in the gravastar limit

$$p = \epsilon \left(\frac{y - y_1}{3y_1 - y}\right),\tag{4.2}$$

11

where

$$y(r) = \left[1 - \left(\frac{r}{\alpha}\right)^2\right]^{1/2}, \quad y_1 = y(R).$$
 (4.3)

We measure the radial coordinate r in the unit

$$\alpha = \left(\frac{3}{8\pi\epsilon}\right)^{1/2} = R_{\rm S} \left(\frac{R}{R_{\rm S}}\right)^{3/2}.\tag{4.4}$$

In terms of (4.3), (2.4) and (3.4) take the form

$$j = \frac{2y}{|3y_1 - y|}, \qquad \frac{2m(r)}{r} = 1 - y^2. \tag{4.5}$$

We will find it convenient to introduce the new independent variable [44]

$$x \equiv 1 - y = 1 - \left[1 - \left(\frac{r}{\alpha}\right)^2\right]^{1/2},$$
 (4.6)

together with the parameter κ given by

$$\kappa \equiv 3\sqrt{1 - \frac{R^2}{\alpha^2}} - 1 = 3y_1 - 1. \tag{4.7}$$

In terms of the variables (κ, x) , the HT equations (3.3), (3.8), (3.9), (3.14) and (3.15) take the following forms

$$x(2-x)(x+\kappa)\frac{d^{2}\varpi}{dx^{2}} + \left[5k + (3-5\kappa)x - 4x^{2}\right]\frac{d\varpi}{dx} - 4(\kappa+1)\varpi = 0(4.8)$$

$$\frac{dm_0}{dx} = \alpha^3 \frac{(1-x)[x(2-x)]^{3/2}}{(\kappa+x)^2} \left[\frac{1}{3} x(2-x) \left(\frac{d\varpi}{dx} \right)^2 + \frac{8(\kappa+1)}{3(\kappa+x)} \varpi^2 \right], \quad (4.9)$$

$$\frac{1}{\alpha^2} \frac{dp_0^*}{dx} = -\frac{\kappa + 1}{\alpha^2 (1 - x)(\kappa + x)} p_0^* - \left[\frac{2 + (\kappa + 1)(1 - x) - 3(1 - x)^2}{\alpha^3 (\kappa + x)(1 - x)^2 [x(2 - x)]^{3/2}} \right] m_0
+ \frac{8x(2 - x)}{3(\kappa + x)^2} \varpi \left(\frac{d\varpi}{dx} \right) - \frac{8 \left[1 - (\kappa + 1)(1 - x) \right]}{3(\kappa + x)^3} \varpi^2
+ \frac{\left[x(2 - x) \right]^2}{3(1 - x)(\kappa + x)^2} \left(\frac{d\varpi}{dx} \right)^2,$$
(4.10)

$$\frac{dv_2}{dx} = -\frac{2h_2}{\kappa + x} + \frac{2\left[\alpha x(2-x)\right]^2}{3(\kappa + x)^3} \left[1 + (\kappa + 1)(1-x) - 2(1-x)^2\right] \times \left[\left(\frac{d\varpi}{dx}\right)^2 + \frac{4(\kappa + 1)}{x(2-x)(\kappa + x)}\varpi^2\right],$$
(4.11)

$$\frac{dh_2}{dx} = \frac{(1-x)^2 + (\kappa+1)(1-x) - 2}{x(2-x)(\kappa+x)} h_2 - \frac{2(\kappa+x)}{[x(2-x)]^2} v_2
+ \alpha^2 \left[2x^2(2-x)^2 - (\kappa+x)^2 \right] \frac{x(2-x)}{3(\kappa+x)^3} \left(\frac{d\varpi}{dx} \right)^2
+ 4\alpha^2 \left[2x^2(2-x)^2 + (\kappa+x)^2 \right] \frac{(\kappa+1)}{3(\kappa+x)^4} \varpi^2.$$
(4.12)

Equations (4.8)-(4.12) must be supplemented by the relations (3.10), (3.20) and (3.21) which now take the form

$$h_0^- - \frac{4x(2-x)\alpha^2}{3(\kappa+x)^2}\varpi^2 + p_0^* = h_c, \tag{4.13}$$

$$h_2 + \frac{4x(2-x)\alpha^2}{3(\kappa+x)^2}\varpi^2 + p_2^* = 0, (4.14)$$

$$m_{2} = \alpha^{3} (1 - x)^{2} \left[x(2 - x) \right]^{1/2} \left\{ \frac{2x^{3} (2 - x)^{3}}{3(\kappa + x)^{2}} \left[\left(\frac{d\varpi}{dx} \right)^{2} + \frac{4(\kappa + 1)\varpi^{2}}{x(2 - x)(\kappa + x)} \right] - \frac{h_{2}}{\alpha^{2}} \right\}.$$

$$(4.15)$$

Solutions to equations (4.8)-(4.12) must match at the surface Σ with the exterior solutions (3.5), (3.11), (3.13), (3.17) and (3.18), such that

$$\overline{\omega}_1 = \Omega - \frac{2J}{\alpha^3 (1 - y_1^2)^{3/2}},\tag{4.16}$$

$$(m_0)_1 = \delta M - \frac{J^2}{\alpha^3 (1 - y_1^2)^{3/2}} - 8\pi \alpha^3 (1 - y_1^2)^{3/2} \left(\frac{R}{2M} - 1\right) \epsilon(R) (p_0^*)_1, \tag{4.17}$$

$$(h_0)_1 = -\frac{(m_0)_1}{\alpha y_1^2 (1 - y_1^2)^{1/2}},\tag{4.18}$$

$$(h_2)_1 = \frac{3 - y_1^2}{\alpha^4 (1 - y_1^2)^3} J^2 + KQ_2^2(\zeta), \tag{4.19}$$

$$(v_2)_1 = -\frac{J^2}{\alpha^4 (1 - y_1^2)^2} + K \left(\frac{1 - y_1^2}{y_1}\right) Q_2^1(\zeta), \tag{4.20}$$

where $\zeta = (1 + y_1^2)/(1 - y_1^2)$ and the subscript 1 indicates the value of the function at the surface $x_1 = 1 - y_1$. Finally, in terms of the variable x, (3.24) and (3.25) read now

$$\xi_0(x) = \frac{\alpha(1-x)(\kappa+x)}{[x(2-x)]^{1/2}} p_0^*, \tag{4.21}$$

$$\xi_2(x) = \frac{\alpha(1-x)(\kappa+x)}{[x(2-x)]^{1/2}} p_2^*, \tag{4.22}$$

$$\varepsilon(x) = \frac{3(1-x)(\kappa+x)}{2x(2-x)} \left[h_2(x) + \frac{4x(2-x)\alpha^2}{3(\kappa+x)^2} \varpi^2 \right] - \frac{3}{2} (v_2 - h_2), \quad (4.23)$$

where in (4.23) we have substituted p_2^* for its value given by (4.14).

5. Methods and results

In this section, we present our results of surface and integral properties for slowly rotating Schwarzschild stars, at second order in the angular frequency Ω . We numerically integrated the HT structure equations for different values of the parameter $R/R_{\rm S}$, in the regime beyond the Buchdahl limit $1 < R/R_{\rm S} < 9/8$, by using a standard Runge-Kutta algorithm. In order to show the whole sequence of slowly rotating Schwarzschild stars in adiabatic and quasi-stationary contraction, and also as a consistency check, we include results for stars above the Buchdahl limit, i.e. $R/R_{\rm S} \ge 9/8$, which were reported by [44] and confirmed by [41]. As another consistency check, we constructed codes that solve the HT equations for the Schwarzschild star in the original (r, R) coordinates using analogous procedures, and the computed values of the surface parameters agree. More information about the relative differences between the parameters computed in (κ, x) and (r, R) can be found in Appendix B. We use dimensionless variables where the units in which the quantities are expressed are given in the corresponding descriptions. In Table 1 we list the surface properties for some selective values of $R/R_{\rm S}$. The main results are presented further in figures 1-16.

The regime where the parameter $R/R_{\rm S}$ goes beyond the Buchdahl limit, i.e. $1 < R/R_{\rm S} < 9/8$, requires some careful analysis due to the presence of the singular radius R_0 (2.13). In order to consider this region, [41] imposed the condition $\kappa = |3y_1 - 1|$ (see equation (48) there); however, as it was pointed out by [45], that assumption turned out to be erroneous which marred the results of the surface and integral properties in the regime beyond the Buchdahl limit. However, as we show in the following sections, in the gravastar limit as $R \to R_{\rm S}$, the results reported in [41] agree with the ones we are presenting here. In the following, we reconsider the analysis carried out by [41], and we study with more detail the behavior of the structure equations at the infinite pressure surface.

Before proceeding further, it is crucial to clarify the range of values of the relevant quantities. We have that in the regime beyond the Buchdahl limit, $1 < R/R_S < 9/8$, $\kappa \in (-1,0)$, where $\kappa = 0$ corresponds to the Buchdahl radius $R/R_S = 9/8$, and $\kappa = -1$ is the Schwarzschild limit $R = R_S$. Some relevant values of x are the following

$$\begin{cases} x = 0, & \text{centre of the star,} \\ x_0 = -\kappa, & \text{surface with divergent pressure,} \\ x_1 = (2 - \kappa)/3, & \text{surface of the star.} \end{cases}$$

Note that in the region beyond the Buchdahl limit, the stellar surface $x_1 \in (2/3, 1)$. Since we are considering this regime here, we have to clarify the region of interest for the integrations. We are primarily concerned with the region with positive pressure, i.e., $x_0 < x \le x_1$. Regarding the negative pressure region, $0 < x < x_0$, which emerges once we cross the Buchdahl limit, we will examine the implications of extending the solutions inside the surface x_0 . The inward extension is not necessary for evaluation of any exterior properties, but it allows for comparison with the interior analytic rotating gravastar solutions.

For configurations with $R/R_S \ge 9/8$, the analysis is simpler because there is no x_0 , so the integrations cover the whole interior of the star $0 < x < x_1$. The boundary conditions for that situation have already been discussed thoroughly in [41, 44], so we will not repeat that here.

Table 1. Surface properties of slowly rotating Schwarzschild stars, for some selective values of $R/R_{\rm S}$. The main results are displayed in the accompanying figures. We employ the same units introduced by [44], where we include the corresponding factors c and G in case one wishes to recover the physical parameters. The stellar radius is measured in units of the Schwarzschild radius $R_{\rm S} \equiv 2GM/c^2$. The normalized moment of inertia $\tilde{I} \equiv I/MR^2$ is dimensionless; the change in mass $\delta M/M$ is measured in the unit $(GJ/R_{\rm S}^2c^3)^2$; the 'Kerr factor' $\tilde{Q} \equiv QM/J^2$ is dimensionless; the surface angular velocity ϖ_1 , relative to the local inertial frame, is measured in the unit $GJ/R_{\rm S}^3c^2$; ξ_0 (l=0 deformation) in the unit $(GJ)^2/R_{\rm S}^3c^6$; ξ_2 (l=2 deformation) in the unit $(GJ)^2/R_{\rm S}^3c^6$; the ellipticity ε is measured in units of $(GJ/R_{\rm S}^2c^3)^2$.

$R/R_{\rm S}$	$ ilde{I}$	$\delta M/M$	\widetilde{Q}	$\overline{arpi_1}$	ξ_0	ξ_2	ε
1.001	0.9980	2.0000	1.0000	0.0059	-0.0059	-0.0060	5.9880
1.010	0.9803	2.0000	1.0000	0.0588	-0.0593	-0.0610	5.8860
1.087	0.8493	2.0471	1.0062	0.4356	-0.4255	-0.6555	5.5517
1.123	0.8015	2.1667	1.0201	0.5663	-0.4758	-1.0487	5.7831
1.125	0.7991	2.1783	1.0212	0.5727	-0.4739	-1.0731	5.8034
1.150	0.7719	2.3479	1.0381	0.6439	-0.4240	-1.3941	6.0901
1.490	0.6032	4.8430	1.6111	0.8887	1.0245	-6.3423	9.8158

5.1. Dragging of the inertial frames and moment of inertia

The dragging of the inertial frames can be obtained from equation (4.8), which has regular singular points at x = 0 and $x = -\kappa$, in the region of interest. The relevant singularity, beyond the Buchdahl limit, at which we apply boundary conditions is $x_0 = -\kappa$, and it will be the starting point of our numerical integration. In Appendix A we discuss a series solution to (4.8), which was discussed first by [47], that can be used to seed the numerical integration slightly past the singular point, but only one of the solutions results in finite behavior of the second order perturbation functions at $x_0 = -\kappa$. The appropriate solution of (4.8) has the following behavior near x_0 [see equation (A.5)],

$$\varpi = \varpi_0(\kappa + x)^2 + \mathcal{O}\left((x + \kappa)^3\right),\tag{5.1}$$

where we are measuring ϖ in units of ϖ_0 , which is arbitrary. We numerically integrated (4.8), with the boundary condition (5.1), starting from x_0 (or rather from $x_0 + \epsilon$, with a cut-off value $\epsilon \sim 10^{-7}$), up to the stellar surface x_1 , for various values of the parameter $R/R_{\rm S}$ in the regime beyond Buchdahl $1 < R/R_{\rm S} < 9/8$. As a code test, we computed the surface value ϖ_1 for a star with $R/R_{\rm S} = 1.12499$, very close to the Buchdahl radius $R_{\rm B} = (9/8)R_{\rm S}$, and we obtained $\varpi_1 = 0.57267$, which is in very good agreement with

the value reported in [44] at $R_{\rm B}$ (see Table 1 there). The agreement between the (κ, x) and analogous (r, R) codes is extremely good for the frame dragging, with average error for ϖ_1 on the order of 10^{-8} (see Appendix B).

We are following the same conventions as [44] where ϖ is measured in units of J/R_S^3 , thus it will be useful to introduce the following quantities

$$\widetilde{\varpi} \equiv \frac{\varpi}{(J/R_{\rm S}^3)}, \quad \widetilde{\Omega} \equiv \frac{\Omega}{(J/R_{\rm S}^3)}.$$
 (5.2)

In the left-hand panel of figure 1 we present the radial profiles of the angular velocity $\widetilde{\omega}$,

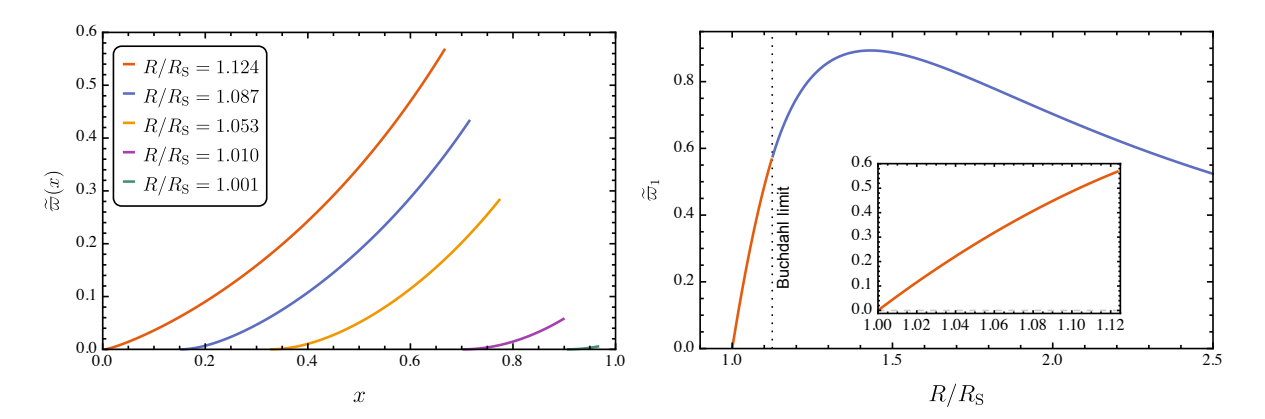


Figure 1. Left panel: Radial profile of the angular velocity $\widetilde{\varpi}$, relative to the local inertial frame (as measured by a distant observer), for various Schwarzschild stars beyond the Buchdahl limit. Each curve starts at its corresponding x_0 value and ends at its corresponding radius x_1 . Right panel: Surface angular velocity $\widetilde{\varpi}_1$, as a function of $R/R_{\rm S}$. The inset zooms in the regime beyond the Buchdahl limit $1 < R/R_{\rm S} < 9/8$. Our results for Schwarzschild stars above Buchdahl, i.e. $R/R_{\rm S} > 9/8$, are in very good agreement with those reported in [44]. Note the smooth match of $\widetilde{\varpi}$ at the Buchdahl radius, and subsequent approach to zero as $R \to R_{\rm S}$.

relative to the local inertial frame, for various values of the parameter $R/R_{\rm S}$. Note that each curve starts at its corresponding x_0 value and ends at its corresponding radius x_1 , thus each profile corresponds to the positive pressure region $x_0 < x \le x_1$. We observe that $\widetilde{\varpi}$ is well-behaved and it grows monotonically with x from x_0 . We also observe how the positive pressure region of the star shrinks as $R/R_{\rm S}$ approaches the gravastar limit. In the limit $R \to 2M$, $x_0 = x_1$, then this region practically disappears to become a boundary layer at the Schwarzschild radius, leaving behind a gravastar in the whole interior $x < x_0$ [34].

In the right-hand panel of figure 1 we display the surface value of the angular velocity $\widetilde{\varpi}_1 = \widetilde{\varpi}(x_1)$, as a function of the parameter $R/R_{\rm S}$. The inset magnifies the region beyond the Buchdahl radius. We observe that $\widetilde{\varpi}_1$ has a local maximum when $R/R_{\rm S} \sim 1.4$, it is well-behaved and matches smoothly at the Buchdahl bound. Moreover, in the limit as $R \to R_{\rm S}$, $\widetilde{\varpi}_1 \to 0$; therefore we have that in the gravastar limit

$$\varpi \to 0, \quad \Rightarrow \quad \omega = \Omega,$$
(5.3)

in agreement with [45]. We point out that $\widetilde{\varpi}_1$ does not reach exactly zero in agreement with a theorem due to Hartle [42]. For instance, for $R/R_{\rm S}=1.000001$, we obtain $\widetilde{\varpi}_1 \sim 10^{-6}$. Nevertheless, as it was shown in [45], it is expected that in the strict gravastar limit $R=R_{\rm S}$, $\widetilde{\varpi}_1=0$, however, we cannot consider exactly that limit in our numerical approach. These results improve those reported by [41] where there was a kink at the Buchdahl bound due to the wrong assumption of the absolute value of κ (see figure 5 there). However, in the Schwarzschild limit $R \to R_{\rm S}$, the results are essentially the same.

In figure 2 we present the radial profiles of the 'dragging' function $\omega(x)$, normalized by the angular velocity Ω , for some selective values of the parameter $R/R_{\rm S}$. Each curve starts (ends) at its corresponding x_0 (x_1) value. Note that the dragging is maximum at the center, it is 1 exactly on x_0 by virtue of the fact that $\varpi \to 0$, and it decreases as we move outwards from x_0 up to the surface x_1 . Thus, the dragging of the inertial frames is maximum at the 'origin' x_0 . This is consistent with other results for relativistic stars [43, 51]. In figure 3 we show the angular velocity of the star $\widetilde{\Omega}$, as a function of

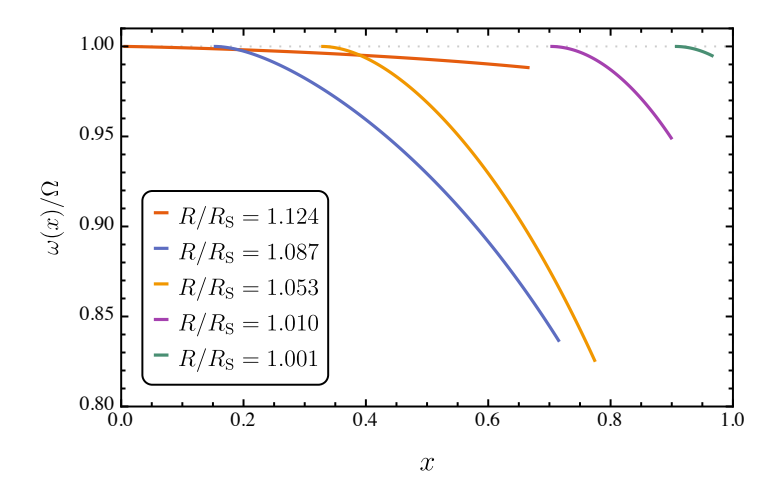


Figure 2. Radial profile of the dragging of the inertial frames $\omega(x)/\Omega$, for various Schwarzschild stars in the regime beyond the Buchdahl limit $1 < R/R_{\rm S} < 9/8$. Note that the dragging is maximum at x_0 , but it is always less than 1 outside x_0 .

the parameter $R/R_{\rm S}$. The inset zooms into the region beyond the Buchdahl limit. We observe that $\widetilde{\Omega}$ grows monotonically as the compactness increases, and it is finite and continuous at the Buchdahl bound. Moreover, as $R \to R_{\rm S}$ we observe that $\widetilde{\Omega} \to 2$, thus we conclude that in the gravastar limit

$$\Omega = \omega = \frac{2J}{R_S^3},\tag{5.4}$$

which agrees with the exterior HT solution (3.6), when $r \to R_{\rm S}$. These results improve those we presented in [41] (see figure 7 there), where $\widetilde{\Omega}$ went above the value 2, but then it decreased approaching 2 in the gravastar limit. However, as we found before, in the relevant gravastar limit our results here are practically the same as those reported by [41]. The left-hand panel of figure 4 shows the dimensionless moment of inertia $\overline{I} \equiv I/M^3$,

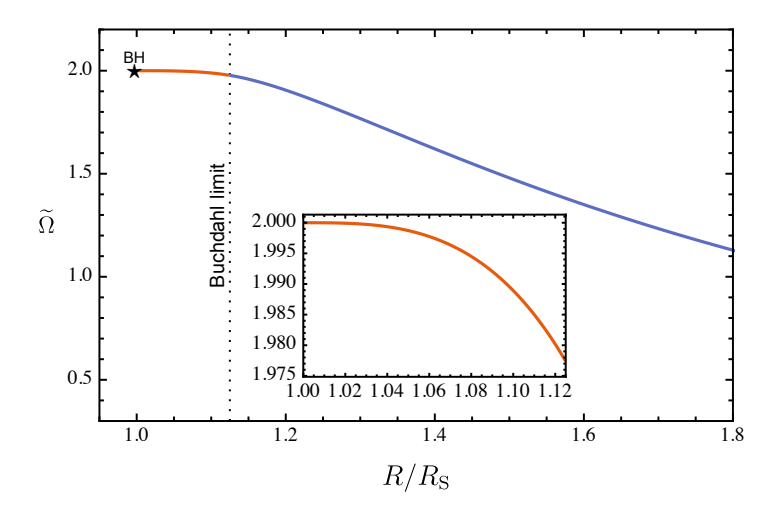


Figure 3. Angular velocity of the star Ω (in units of $J/R_{\rm S}^3$), relative to the distant observers, as a function of the parameter $R/R_{\rm S}$. The inset enhances the region beyond the Buchdahl limit $1 < R/R_{\rm S} < 9/8$. Note the approach to the value $\Omega = 2J/R_{\rm S}^3$, as $R \to R_{\rm S}$.

as a function of the parameter $R/R_{\rm S}$. The quantity \bar{I} turns out to be relevant in the context of the I-Love-Q relations [52, 53]. We observe that \bar{I} decreases monotonically as the compactness increases, and it is continuous at the Buchdahl radius. In the gravastar limit, as $R \to R_{\rm S}$, $\bar{I} \to 4$, corresponding to the BH value. In the right-hand panel of the same figure we display the normalized moment of inertia $\tilde{I} \equiv I/MR^2$, as a function of the parameter $R/R_{\rm S}$. We observe that \tilde{I} is finite and continuous at the Buchdahl limit where we obtain $\tilde{I} = 0.7992$, which agrees with the value reported in [44]. Moreover, as $R \to R_{\rm S}$, $\tilde{I} \to 1$; thus, in the gravastar limit

$$I = MR^2. (5.5)$$

Notably, this result corresponds to the moment of inertia ascribed to a Kerr black hole. However, for any system satisfying $p = -\epsilon$, the 'fluid angular velocity' parameter Ω drops out of the bulk HT equations and becomes ambiguous. As such, the definition of the moment of inertia for Kerr black holes, or for the gravastar in [45], uses the value of frame dragging on the null hypersurface $I = J/\omega_H$ rather than the standard $I = J/\Omega$. In our numerical approach, we can use the standard definition of the moment of inertia and track its limit, which shows how the two definitions agree on the limit.

Note that in our approach, we are contracting the Schwarzschild star from above, where R approaches $R_{\rm S}$ via an adiabatic and quasi-stationary process. Thus, all the integral and surface properties are computed in the region $x_0 < x < x_1$, which in the gravastar limit $R \to R_{\rm S}$, it becomes essentially a boundary layer located at the Schwarzschild radius where $x_0 = x_1$. Therefore, the moment of inertia (5.5), is being carried out by this boundary layer, while the interior de Sitter region with negative pressure carries no angular momentum [45]. Similar to what we found for the dragging function, these results improve those we reported in [41], where we observed a kink at the Buchdahl limit (see figure 9 there). However, in the gravastar limit, the results are

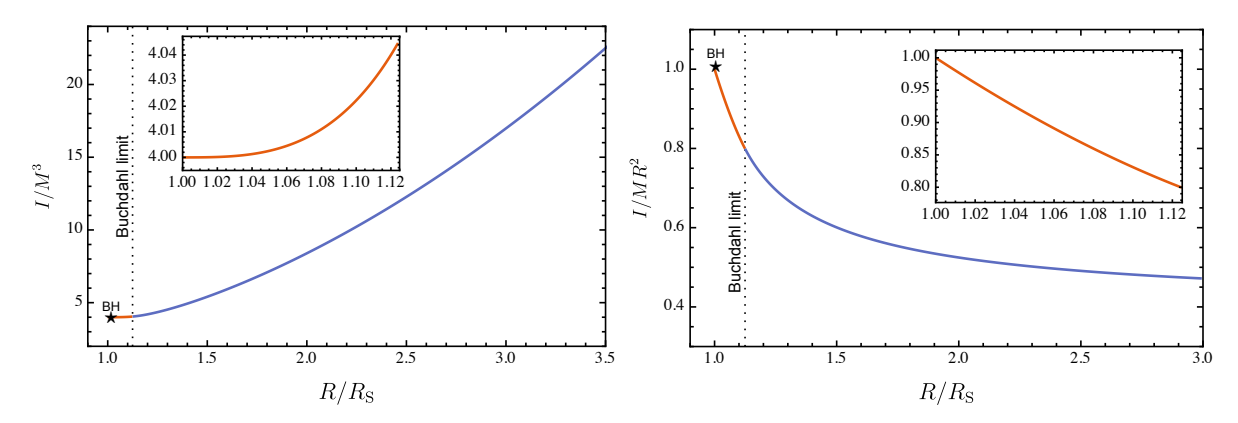


Figure 4. Moment of inertia of Schwarzschild stars. Left panel: Dimensionless moment of inertia $\bar{I} \equiv I/M^3$, as a function of $R/R_{\rm S}$. Note the continuous behaviour at the Buchdahl limit, and the subsequent approach to the BH limit $\bar{I}=4$ as $R\to R_{\rm S}$. Right panel: Same values of I as in the left-hand panel, but now normalized as $\tilde{I} \equiv I/MR^2$, as a function of $R/R_{\rm S}$. The inset zooms into the region beyond the Buchdahl limit $R_{\rm S} < R < (9/8)R_{\rm S}$. Note that \tilde{I} is well-behaved at the Buchdahl limit and it approaches the black hole value $\tilde{I}=1$, as $R\to R_{\rm S}$.

the same.

5.1.1. Inward continuation of the ϖ solution Near x=0, the solution for ϖ can be expanded as [47]

$$\varpi = A \sum_{i=0}^{\infty} a_i x^i + B x^{-\frac{3}{2}} \sum_{i=0}^{\infty} k_i x^i,$$
 (5.6)

where A and B are constants and $a_0 = k_0 = 1$. If we want ϖ to be finite at the origin we must set B = 0. Doing this and integrating outward typically leads to a nonzero value for ϖ on the infinite pressure surface x_0 , implying the presence of a $C_2\varpi_2$ term [see equations (A.8) and (A.11)] and giving the higher order perturbation functions divergences [47] [see for instance, equation (A.13)].

Conversely, integrating ϖ backward from x_0 with a nonzero C_1 , but zero C_2 , like we use outside the infinite pressure surface, leads to nonzero B and diverging ϖ at the origin. These behaviors are illustrated in figure 5 for an example value of $\kappa = -0.5$. It is noteworthy that the $x^{-3/2}$ divergence in ϖ with nonzero B corresponds to a r^{-3} divergence, which has the same behavior as a W_2 term in the analytic slowly rotating gravastar solution from [45]. The solution

$$\varpi = 0, \qquad 0 \le x < -\kappa, \tag{5.7}$$

is special because it both goes to zero at x_0 and does not diverge at the origin. The surface x_0 is both a spacetime singularity and a coordinate singularity, manifesting as a singularity in (4.8). Since the Wronskian $\varpi_1\varpi_2'-\varpi_1'\varpi_2=0$ at $x=-\kappa$, the uniqueness theorem is violated there. Therefore, it is possible that there may be different series solutions on each side of the singularity. Following a suggestion by P. Gondolo, we join

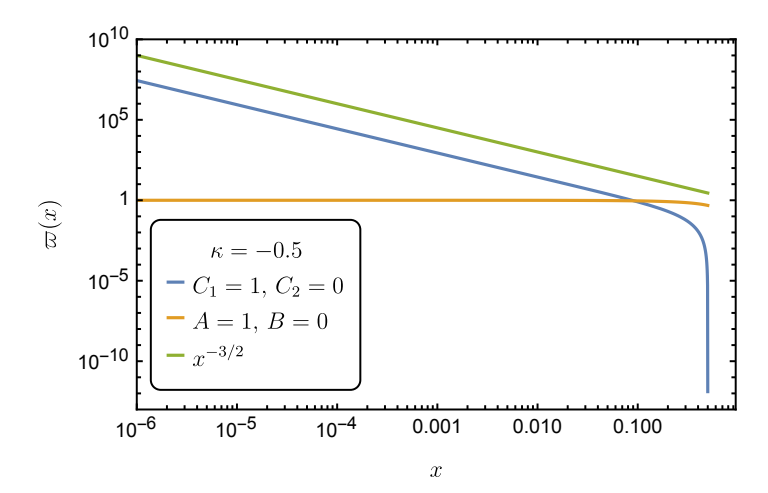


Figure 5. Log-Log plot showing the results of outward integration with A = 1, B = 0 and inward integration with $C_1 = 1, C_2 = 0$ for $\kappa = -0.5$. We see that while A = 1, B = 0 is finite at the origin, it is nonzero at the infinite pressure surface which would lead to divergences in the higher order perturbation functions. Conversely, $C_1 = 1, C_2 = 0$ is zero on the infinite pressure surface such that the higher order perturbation functions may be finite there, but leads to a $x^{-3/2}$ or equivalently r^{-3} type divergence at the origin.

 $\varpi=0$ inside the infinite pressure surface to the ϖ_1 series outside the infinite pressure surface. This is a C1 match. Therefore we use

$$\varpi = 0, \quad 0 < x < -\kappa; \qquad \lim_{x \to -\kappa^+} (\varpi) = \varpi_1, \tag{5.8}$$

to extend the frame dragging function inside the infinite pressure surface, from which we can attempt to compute the other functions.

5.2. Spherical deformations of the star

The spherical deformations of the star can be studied from equations (4.9) and (4.10) for the l=0 sector. As we briefly review in Appendix A, m_0 is divergent at x_0 if a non-zero function of ϖ goes into the R.H.S of (4.9), i.e. if a nonzero contribution from ϖ_2 is present. However, using only the ϖ_1 branch, as we have done in the previous subsection 5.1, allows for well behaved monopole perturbations from the infinite pressure surface outwards. Thus, in terms of the solution (5.1), equations (4.9) and (4.10) can be integrated for m_0 and p_0^* , with the following behaviors near x_0

$$m_0 = \frac{4}{3}(\kappa + 1)[-\kappa(\kappa + 2)]^{5/2}(\kappa + x)\alpha^3 \varpi_0^2 + \mathcal{O}((x + \kappa)^2), \qquad (5.9)$$

$$p_0^* = -\frac{[2\kappa(2+\kappa)]^2}{3(1+\kappa)}(\kappa+x)(\alpha\varpi_0)^2 + \mathcal{O}\left((x+\kappa)^2\right).$$
 (5.10)

We integrated numerically (4.9) and (4.10) in the range $x_0 < x \le x_1$, for various values of the parameter R/R_S , with the boundary conditions (5.9) and (5.10), which are motivated by the following: from (5.27) we have $m_0 = \text{const.}$, inside the infinite pressure

surface. Having it to be nonzero, approaching the surface from outside, either means a point mass at the origin and a continuous m_0 , or a discontinuous m_0 and a δ -function discontinuity in the RHS of (3.8). In order not to make the notation so cumbersome, it will be useful to introduce the following conventions

$$\widetilde{h_0} \equiv \frac{h_0}{(J^2/R_S^4)}, \quad \widetilde{m_0} \equiv \frac{m_0}{(J^2/R_S^3)}, \quad \widetilde{p_0^*} \equiv \frac{p_0^*}{(J^2/R_S^4)}.$$
 (5.11)

In the left-hand panel of figure 6, we present the radial profiles of the perturbation

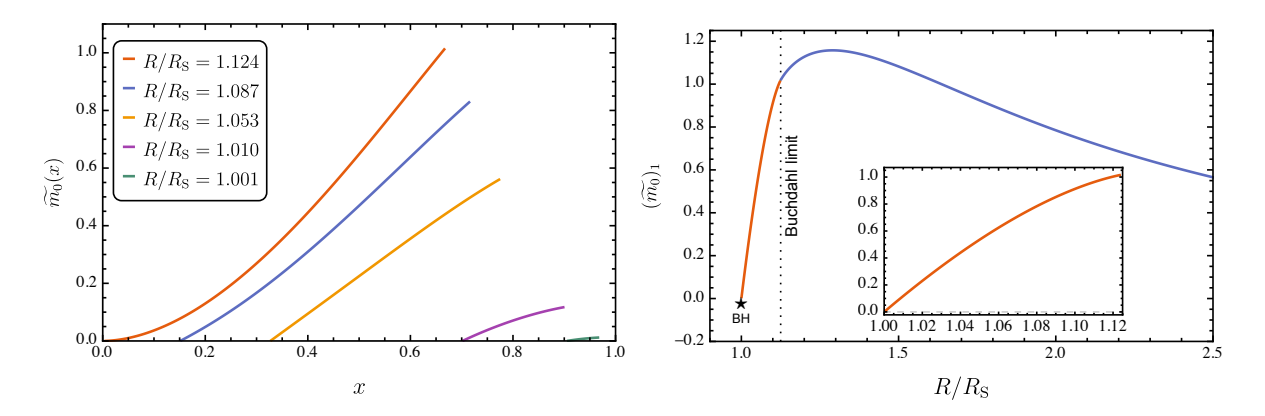


Figure 6. Left panel: Radial profile of the 'mass perturbation' function \widetilde{m}_0 , for some selective values of the parameter $R/R_{\rm S}$. Right panel: Surface value $(\widetilde{m}_0)_1$, as a function of the parameter $R/R_{\rm S}$. The inset zooms into the region beyond the Buchdahl limit $1 < R/R_{\rm S} < (9/8)$. Note that $(\widetilde{m}_0)_1$ has a maximum at $R/R_{\rm S} \sim 1.3$. In the gravastar limit $R \to R_{\rm S}$, $(\widetilde{m}_0)_1 \to 0$.

function $\widetilde{m_0}$, for some selective values of the parameter $R/R_{\rm S}$. The various curves start at their corresponding value x_0 , extending up to their corresponding boundary value x_1 . We observe that $\widetilde{m_0}(x)$ is finite and continuous in the whole range $x_0 < x \le x_1$. In the right-hand panel of the same figure, we display the value of $\widetilde{m_0}$ at the boundary $(\widetilde{m_0})_1 = \widetilde{m_0}(1)$, as a function of $R/R_{\rm S}$. We include results for configurations above the Buchdahl limit, $R/R_{\rm S} > 9/8$, where we observe that as $R/R_{\rm S}$ approaches the Buchdahl limit (from the right), $(\widetilde{m_0})_1$ grows monotonically until it reaches a maximum when $R/R_{\rm S} \sim 1.3$ in agreement with [44]. We notice that $(\widetilde{m_0})_1$ is continuous and matches smoothly at the Buchdhal limit; moreover, in the limit $R/R_{\rm S} \to 1$, $(\widetilde{m_0})_1 \to 0$. Thus, in the gravastar limit

$$m_0 = 0.$$
 (5.12)

In the left-hand panel of figure 7 we present the radial profiles of the 'pressure perturbation' function $\widetilde{p_0^*}$, for various values of $R/R_{\rm S}$. Same as before, each curve starts (ends) at its corresponding x_0 (x_1) value. We observe that $\widetilde{p_0^*}$ is negative, finite, and continuous in the whole corresponding range $x_0 < x \le x_1$. In the right-hand panel of the same figure, we plot the surface value ($\widetilde{p_0^*}$)₁ = $\widetilde{p_0^*}$ (1), as a function of the parameter $R/R_{\rm S}$. We observe that ($\widetilde{p_0^*}$)₁ shows a local maximum at $R/R_{\rm S} \sim 1.8$, and it goes negative for $R/R_{\rm S} < 1.3$ in agreement with [44, 48]. Note that ($\widetilde{p_0^*}$)₁ is finite and

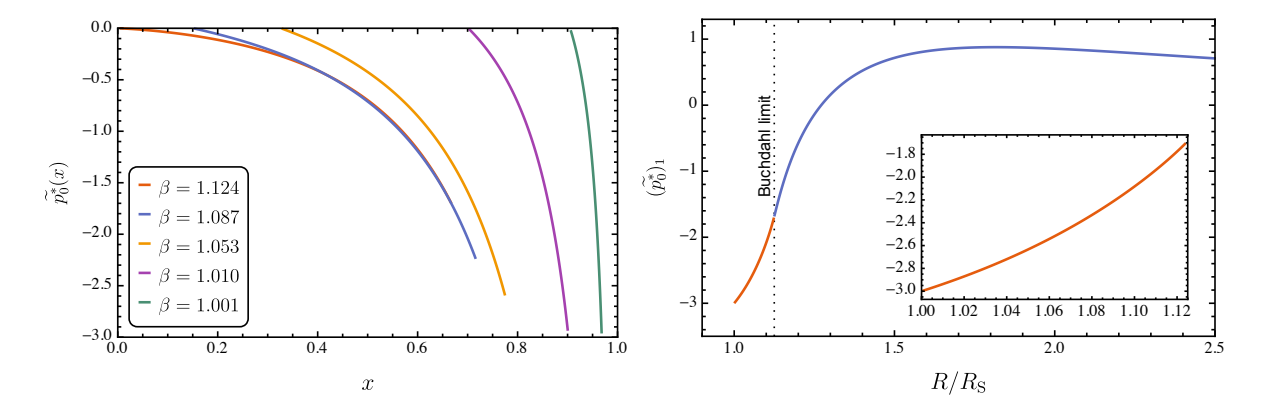


Figure 7. Left panel: Radial profile of the 'pressure perturbation' function $\widetilde{p_0^*}$, for various values of $R/R_{\rm S}$. **Right panel:** surface value $\widetilde{p_0^*}(1) = (\widetilde{p_0^*})_1$, as a function of the parameter $R/R_{\rm S}$. Observe that $(\widetilde{p_0^*})_1$ is finite and matches continuously at the Buchdahl limit; in the gravastar limit $R/R_{\rm S} \to 1$, $\widetilde{p_0^*}(1) \to -3$.

continuous across the Buchdahl limit; moreover, in the limit as $R/R_S \to 1$ we find that $(\widetilde{p_0^*})_1 \to -3$. Thus, in the gravastar limit, we have

$$p_0^* = -\frac{3J^2}{R_S^4}. (5.13)$$

Having obtained the value of the perturbation function p_0^* in the gravastar limit, we can determine the constant h_c in (4.13) which can be rewritten as

$$h_c = h_0^-(x) - H_0(x), (5.14)$$

where

$$H_0(x) = \frac{4x(2-x)}{3(\kappa+x)^2}\alpha^2\varpi^2 - p_0^*.$$
(5.15)

At the stellar surface $x = x_1$, or r = R, continuity of h_0 gives

$$h_c(R) = h_0^+(R) - H_0(R). (5.16)$$

In figure 8 we display the function H_0 , evaluated at the surface, as a function of the parameter $R/R_{\rm S}$. We observe that as the compactness increases, H_0 increases monotonically, until it reaches a local maximum when $R/R_{\rm S}=1.065$ (it is noteworthy that the maximum occurs beyond the Buchdahl limit). In the limit as $R/R_{\rm S} \to 1$, $H_0 \to 3$; thus in the gravastar limit we have

$$H_0(R) = \frac{3J^2}{R_S^4}. (5.17)$$

Figure 9 shows the profile of $\widetilde{h_c} \equiv h_c/(J^2/R_{\rm S}^4)$, as a function of the parameter $R/R_{\rm S}$. We observe that $\widetilde{h_c}$ increases negatively as the compactness of the star increases, reaching a local minimum when $R/R_{\rm S} \sim 1.195$. In the limit as $R/R_{\rm S} \to 1$, $\widetilde{h_c} \to -6$, therefore we conclude that in the gravastar limit

$$h_c = -\frac{6J^2}{R_s^4}. (5.18)$$

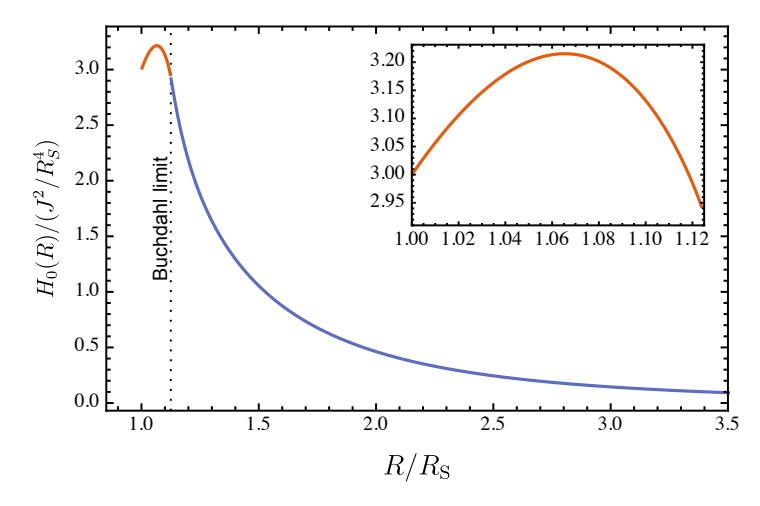


Figure 8. Surface value of the function H_0 , as a function of the parameter $R/R_{\rm S}$. We measure H_0 in units of $J^2/R_{\rm S}^4$. Observe that in the gravastar limit $R/R_{\rm S} \to 1$, $H_0(R) \to 3$.

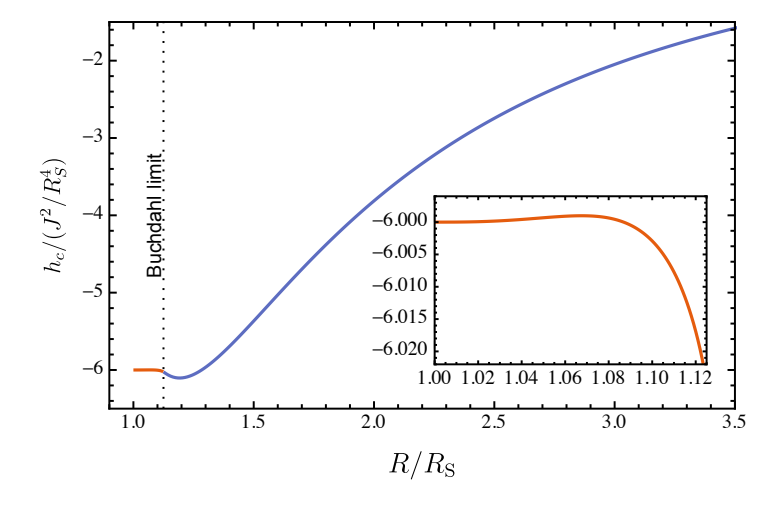


Figure 9. Profile of the constant h_c , as a function of the parameter R/R_S . We measure h_c in units of J^2/R_S^4 . Observe that in the gravastar limit $R/R_S \to 1$, $h_c(R) \to -6$.

The values of m_0 and p_0^* , at the boundary, determine the constant δM associated with the change in mass due to the rotation, as given by (4.17), which in this context can be rewritten as

$$\widetilde{\delta M} = 2\left[(\widetilde{m_0})_1 + \left(\frac{R}{R_S}\right)^{-3} + 3\left(\frac{R}{R_S} - 1\right) (\widetilde{p_0^*})_1 \right], \tag{5.19}$$

where we have introduced

$$\widetilde{\delta M} \equiv \frac{\delta M/M}{(J^2/R_{\rm S}^4)}. (5.20)$$

In figure 10 we show our results for $\widetilde{\delta M}$, as a function of the parameter $R/R_{\rm S}$. In the inset, we enhance the region beyond the Buchdahl bound, $1 < R/R_{\rm S} < (9/8)$. We observe that $\widetilde{\delta M}$ has a local maximum when $R/R_{\rm S} \sim 2.8$, in agreement with [48].

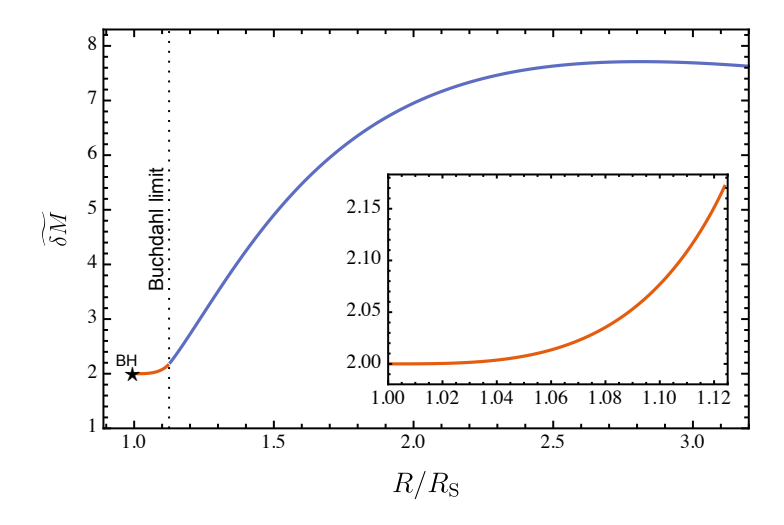


Figure 10. Change of mass $\widetilde{\delta M}$, as a function of the parameter $R/R_{\rm S}$. The inset zooms into the region beyond the Buchdahl limit $1 < R/R_{\rm S} < (9/8)$. Note the smooth approach to the value $\widetilde{\delta M} \to 2$, as $R \to R_{\rm S}$.

Furthermore, $\widetilde{\delta M}$ is well-behaved and continuous at the Buchdahl limit; in the gravastar limit $R \to R_S$, $\widetilde{\delta M} \to 2$, therefore

$$\delta M = \frac{J^2}{R_{\rm S}^3}.\tag{5.21}$$

This result could be already seen from the results of Figs. 6 and 7, where we note that in the gravastar limit $R \to R_S$, $(\widetilde{m_0})_1 \to 0$; thus, in this limit, the first term of the R.H.S of (5.19) vanishes. Regarding the last term on the R.H.S, although $(\widetilde{p_0^*})_1$ is non-zero the term in parenthesis goes to zero as $R \to R_S$, thus we are left only with the second term.

It is noteworthy that (5.12) and (5.21), for the slowly rotating Schwarzschild star in the gravastar limit, match with the corresponding values associated with the Kerr metric. To see this, we recall that the HT exterior solution, as $r \to R_S$, takes the following form [45]

$$m_0 = \delta M - \frac{J^2}{r^3},\tag{5.22}$$

$$h_0 = -\frac{m_0}{r - 2M},\tag{5.23}$$

$$h_2 = \frac{J^2}{r^3} \left(\frac{1}{r} + \frac{1}{M} \right), \tag{5.24}$$

$$m_2 = \frac{J^2(r - 2M)(5M - r)}{Mr^4},\tag{5.25}$$

$$k_2 = -\frac{J^2(r+2M)}{Mr^4},\tag{5.26}$$

which has been shown to be equivalent to the metric for a slowly rotating Kerr BH with mass $M^* = M + \delta M$ and angular momentum J, to order Ω^2 [43]. Note that

in the Schwarzschild limit $r \to R_{\rm S}$, (5.22) and (5.23) agree with (5.12) and (5.21). These results improve those presented in [41] (see figure 11 there) where there seems to appear a maximum in the function $\widetilde{\delta M}$, right after crossing the Buchdahl limit, but then $\widetilde{\delta M}$ went below 2, before reaching the corresponding gravastar limit. However, in the gravastar limit $R \to R_{\rm S}$, both results are practically in agreement.

The behaviour of the perturbation function $\xi_0(R)/R$, as a function of R/R_S , is shown in figure 11. First of all, we corroborate the results reported by [44] when $R/R_S > (9/8)$. We also observe that as the compactness approaches the gravastar limit, $\xi_0(R)/R \to 0$. It is interesting that the quantity $\xi_0(R)/R$ has a local minimum at R = 1.115, slightly below the Buchdahl limit.

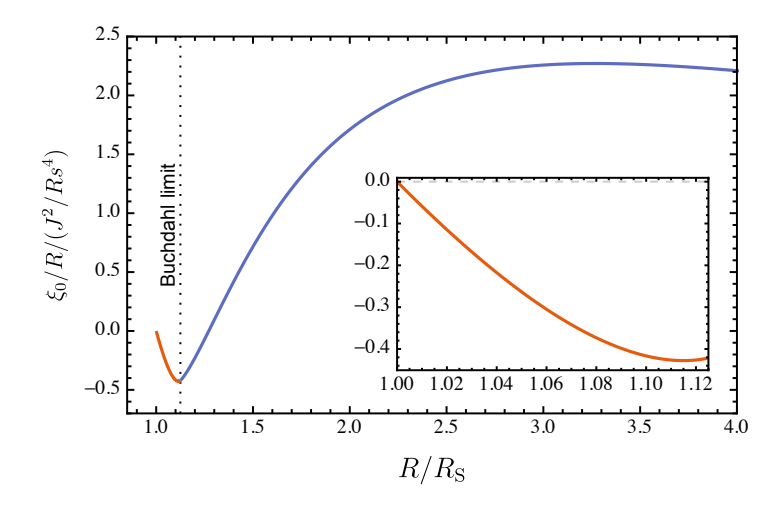


Figure 11. The function $\xi_0(R)/R$, which describes the l=0 deformation of the surface, as a function of the parameter $R/R_{\rm S}$. The function $\xi_0(R)/R$ is measured in the unit $J^2/R_{\rm S}^4$.

5.2.1. Continuation inward of the monopole functions Inside the infinite pressure surface x_0 , using (5.8) into (4.9) we get

$$\frac{dm_0}{dx} = 0, (5.27)$$

Integration, in this region, trivially leads to $m_0 = \text{const.}$ Since we are considering the boundary condition of $\lim_{x\to-\kappa^+}(m_0) = 0$, the most sensible thing to do would be a continuous match§, leaving

$$m_0 = 0,$$
 (5.28)

everywhere inside the surface. Thus, using (5.8) and (5.28), equation (4.10) for p_0^* becomes

$$\frac{dp_0^*}{dx} = -\frac{\kappa + 1}{(1 - x)(\kappa + x)} p_0^*,\tag{5.29}$$

§ A discontinuity in m_0 is related to a δ -function in the energy density which we should not have here.

which can be integrated exactly, giving

$$p_0^* = \frac{c_p(1-x)}{\kappa + x}. (5.30)$$

From the algebraic constraint (4.13) we obtain

$$h_0 = h_c - \frac{c_p(1-x)}{\kappa + x}. (5.31)$$

Finiteness of the perturbation functions requires $c_p = 0$. In many cases, one would also enforce continuity of h_0 , which would set h_c in the interior, but since $e^{2\nu_0} \to 0$ on the infinite pressure surface any finite discontinuity of h_0 will still have a continuous g_{tt} . Thus, strict continuity of h_0 itself may not be necessary.

5.3. Quadrupole deformations of the star

The quadrupole deformations of the star can be studied from equations (4.11) and (4.12), for the l=2 sector, whose solutions can be written as a superposition of a particular integral and a homogeneous part (indicated by the superscripts p and h respectively) in the following form

$$h_2 = h_2^{(p)} + Ah_2^{(h)}, \quad v_2 = v_2^{(p)} + Av_2^{(h)},$$
 (5.32)

where A is a constant. The homogeneous functions are solutions of the following equations

$$\frac{dv_2^{(h)}}{dx} = -\frac{2h_2^{(h)}}{\kappa + x},\tag{5.33}$$

$$\frac{dh_2^{(h)}}{dx} = \frac{(1-x)^2 + (\kappa+1)(1-x) - 2}{x(2-x)(\kappa+x)} h_2^{(h)} - \frac{2(\kappa+x)}{[x(2-x)]^2} v_2^{(h)}.$$
 (5.34)

The following series approximations

$$v_2^{(h)} \approx C + \frac{C(x+\kappa)^2}{8\kappa^2 + 8\kappa^3 + 2\kappa^4} + \frac{C(1+\kappa)(x+\kappa)^3}{\kappa^3 (2+\kappa)^3},$$
 (5.35)

$$h_2^{(h)} \approx -\frac{C(x+\kappa)^2}{8\kappa^2 + 8\kappa^3 + 2\kappa^4} - \frac{3C(1+\kappa)(x+\kappa)^3}{2\kappa^3(2+\kappa)^3},$$
 (5.36)

where C is an arbitrary constant, are regular, satisfy the homogeneous equations (5.33) and (5.34), to order $(x + \kappa)^2$, and can be used for starting the numerical integrations of the homogeneous part of the solution. The particular solutions to equations (4.11) and (4.12) are slightly more difficult to deal with because the ϖ dependent driving terms are divergent. The terms are

$$D_{h_2}(\varpi) \approx \left[-\frac{8\kappa^3 (2+\kappa)^3}{3(x+\kappa)} + \frac{8}{3}\kappa^2 (1+\kappa)(2+\kappa)^2 - 4\kappa (2+\kappa)(x+\kappa) \right] (\alpha \varpi_0)^2,$$

$$(5.37)$$

$$D_{v_2}(\varpi) \approx \left[-\frac{8\kappa^3 (2+\kappa)^3}{3(x+\kappa)} + \frac{16}{3}\kappa^2 (1+\kappa)(2+\kappa)^2 - \frac{8}{3}\kappa (2+\kappa)(x+\kappa) \right] (\alpha \varpi_0)^2,$$

$$(5.38)$$

to linear order in $x + \kappa$. Obtaining these requires that one keep terms in the series for ϖ , at least through a_2 . While these have divergent $(x + \kappa)^{-1}$ terms, it does not mean that h_2 or v_2 are necessarily divergent. The terms dependent on h_2 in (4.11), (4.12) can also generate divergent $(x + \kappa)^{-1}$ terms if $h_2^{(p)} \to \text{const.}$, as $x \to -\kappa$. We therefore postulate

$$h_2^{(p)} \approx \left[h_2^a + h_2^b(x+\kappa) + h_2^c(x+\kappa)^2 \right] (\alpha \varpi_0)^2,$$
 (5.39)

$$v_2^{(p)} \approx \left[v_2^a + v_2^b(x+\kappa) + v_2^c(x+\kappa)^2 \right] (\alpha \varpi_0)^2.$$
 (5.40)

We find that for the following values

$$h_2^a = -\frac{4}{3} \left[\kappa(\kappa + 2) \right]^3, \quad h_2^b = \frac{4}{3} \kappa^2 (\kappa + 1) (\kappa + 2)^2,$$

$$h_2^c = -\frac{2}{3} \kappa (2 + \kappa), \tag{5.41}$$

$$v_2^a = 0, \quad v_2^b = 2h_2^b, \quad v_2^c = h_2^c,$$
 (5.42)

 $h_2^{(\mathrm{p})}$ and $v_2^{(\mathrm{p})}$ satisfy (4.11) and (4.12) with error of the order of $(x+k)^2$.

The particular solutions $h_2^{(p)}$ and $v_2^{(p)}$ are found by integrating (4.11) and (4.12) out from x_0 (or rather from $x_0 + \delta$, where $\delta = 10^{-6}$ is a cut-off value) with the boundary conditions (5.39) and (5.40). Likewise, the homogeneous solutions $h_2^{(h)}$ and $v_2^{(h)}$ can be obtained by integrating (5.33) and (5.34) with the initial behaviours (5.35), (5.36), for an arbitrary value of the constant C. The constant A in (5.32) and the constant K appearing in (3.17), (3.18) and (3.19), can be determined from the matching condition $[h_2] = [v_2] = 0$, as given by equations (4.19) and (4.20). In the following, will be convenient to introduce the following quantities

$$\widetilde{h}_2 \equiv \frac{h_2}{(J^2/R_S^4)}, \quad \widetilde{m}_2 \equiv \frac{m_2}{(J^2/R_S^3)}, \quad \widetilde{k}_2 \equiv \frac{k_2}{(J^2/R_S^4)}.$$
 (5.43)

In the left-hand panel of figure 12 we display the radial profile of the perturbation function $\widetilde{h_2}(x)$, for some selective values of the parameter $R/R_{\rm S}$. Likewise to our previous results, each curve starts (ends) at its corresponding x_0 (x_1) value. We observe that $\widetilde{h_2}(x)$ is finite and continuous along the corresponding range $x_0 < x < x_1$. The right-hand panel of the same figure shows the surface value ($\widetilde{h_2}$)₁ = $\widetilde{h_2}(1)$, as a function of $R/R_{\rm S}$. As before, we also include configurations above the Buchdahl limit, i.e. $R/R_{\rm S} > 9/8$. Note that ($\widetilde{h_2}$)₁ shows a local maximum near $R/R_{\rm S} \sim 1.27$ and it matches continuously at the Buchdahl limit; moreover there is a local minimum ≈ 2.52 below the Buchdahl limit at $R/R_{\rm S} \sim 1.09$, and as $R \to R_{\rm S}$, ($\widetilde{h_2}$)₁ $\to 3$. Thus, we have that in the gravastar limit

$$h_2 = \frac{3J^2}{R_S^4}. (5.44)$$

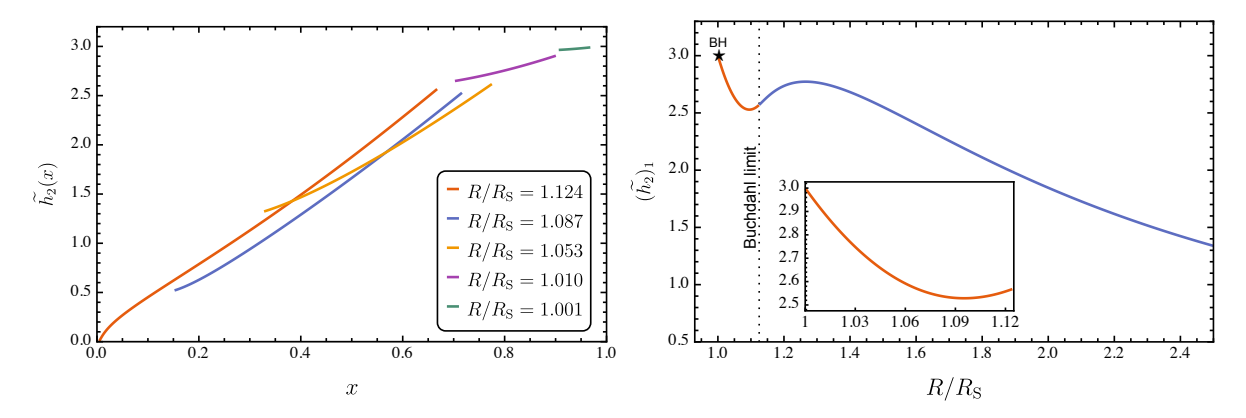


Figure 12. Left panel: Radial profile of the function $\widetilde{h_2}$, for various values of $R/R_{\rm S}$. **Right panel:** surface value $(\widetilde{h_2})_1$, as a function of the parameter $R/R_{\rm S}$. The inset zooms into the regime beyond the Buchdahl limit. Observe that $(\widetilde{h_2})_1$ is finite and matches continuously at the Buchdahl limit; in the gravastar limit $R/R_{\rm S} \to 1$, $(\widetilde{h_2})_1 \to 3$.

This result is consistent with the exterior solution for h_2 , as given by (5.24), when $r \to R_S$. This is expected because the interior and exterior solutions must match continuously at the boundary $\Sigma_0 = R$, i.e., $[h_2] = 0$.

It is interesting that for the interior of the slowly rotating gravastar, [45] found that the function h_2 takes the form

$$h_2 = \frac{2J^2}{rR_S} \left(\frac{1}{r^2} - \frac{1}{R_S^2} \right), \tag{5.45}$$

which vanishes when $r \to R_S$. However, the exterior function h_2 (5.24), evaluated at $r = R_S$, does not vanish; so it seems that in their model the perturbation h_2 , besides being non-regular at r = 0, is discontinuous at the surface. However, the discontinuity in the limit is related to the discontinuity across the infinite pressure surface, which we discuss in the next subsection

The perturbation function $\widetilde{m}_2(x)$, as given by (4.15), is depicted in figure 13 where in the left-hand panel we show its radial profile for various values of the parameter $R/R_{\rm S}$. In the right-hand panel of the same figure, we display the value at the boundary $(\widetilde{m}_2)_1 = \widetilde{m}_2(1)$, as a function of the parameter $R/R_{\rm S}$. We include results for configurations above the Buchdahl limit, where we observe that $(\widetilde{m}_2)_1$ has a local maximum when $R/R_{\rm S} \sim 1.72$. Close to the Buchdahl limit, $(\widetilde{m}_2)_1$ is finite and continuous, moreover, as $R \to R_{\rm S}$ we observe that $(\widetilde{m}_2)_1 \to 0$. Thus, we conclude that in the gravastar limit

$$m_2 = 0,$$
 (5.46)

which agrees with the exterior HT solution for m_2 , equation (5.25), when $r \to R_S$. As before, this is expected from the continuity condition at the surface $[m_2] = 0$. Note that our result also agrees with the surface value of (9.1d) in [45], when $r \to R_H = R_S$, for the interior of the slowly rotating gravastar.

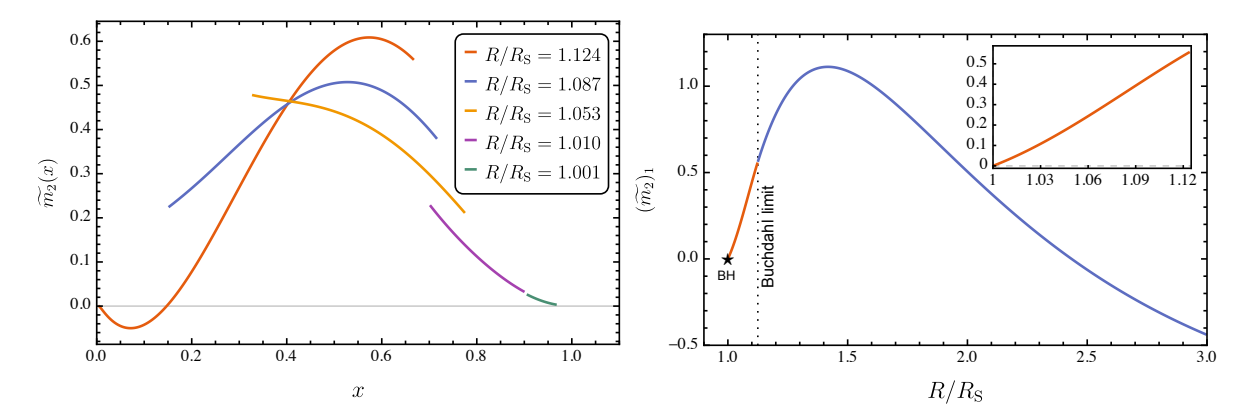


Figure 13. Left panel: Radial profile of the 'mass perturbation' function $\widetilde{m_2}$ for various values of $R/R_{\rm S}$. Right panel: surface value $(\widetilde{m_2})_1 = \widetilde{m_2}(1)$, as a function of the parameter $R/R_{\rm S}$. The inset zooms into the regime beyond the Buchdahl limit. Observe that $(\widetilde{m_2})_1$ is finite and matches continuously at the Buchdahl limit; in the gravastar limit $R/R_{\rm S} \to 1$, $(\widetilde{m_2})_1 \to 0$.

The left-hand panel of figure 14 shows the radial profile of the perturbation function $\widetilde{k}_2(x)$, for different values of the parameter $R/R_{\rm S}$. We observe that $\widetilde{k}_2(x)$ is finite and continuous in the corresponding regions $x_0 < x < x_1$. In the right-hand panel of the same figure, we display the surface value $\widetilde{k}_2(1) = (\widetilde{k}_2)_1$, as a function of $R/R_{\rm S}$. We observe that $(\widetilde{k}_2)_1$ is well-behaved and matches continuously at the Buchdahl limit; furthermore, in the limit as $R \to R_{\rm S}$, $(\widetilde{k}_2)_1 \to -4$. Thus, we conclude that in the gravastar limit

$$k_2 = -\frac{4J^2}{R_S^4},\tag{5.47}$$

which agrees with the exterior HT solution, (5.26), when $r \to R_S$. Our result (5.47) is also in agreement with the surface value for k_2 for the slowly rotating gravastar, equation (9.1f) in [45], when $r \to R_H = R_S$. However, we note that their perturbation function is non-regular as $r \to 0$, which seems to be related to the behavior we find after extending the k_2 function inward as we discuss in the next subsection.

In figure 15 we display the l=2 boundary deformation function $-\xi_2(R)/R$, as a function of $R/R_{\rm S}$. As a verification test, we computed values of $-\xi_2(R)/R$ for configurations above the Buchdahl limit $R/R_{\rm S} > (9/8)$ which are in very good agreement with the results reported by [44]. However, at the Buchdahl radius we obtain $\xi_2(R_{\rm B}) = -1.073(J^2/R_{\rm S}^3)$ which corrects the value reported by [44]. We observe that in the gravastar limit, $-\xi_2(R)/R \to 0$.

In figure 16, we present the ellipticity of the outer boundary ε_1 , as given by equation (4.23), as a function of the parameter $R/R_{\rm S}$. We measure the ellipticity in units of $J^2/R_{\rm S}^4$. We observe that ε shows a local maximum, ≈ 12.18 , at $R/R_{\rm S} \approx 2.32$, in agreement with [44]. There is also a local minimum, ≈ 5.53 , at $R/R_{\rm S} \approx 1.08$ which is beyond the Buchdahl limit. At the Buchdahl radius we obtain $\varepsilon_1(R_{\rm B}) = 5.8033$, which

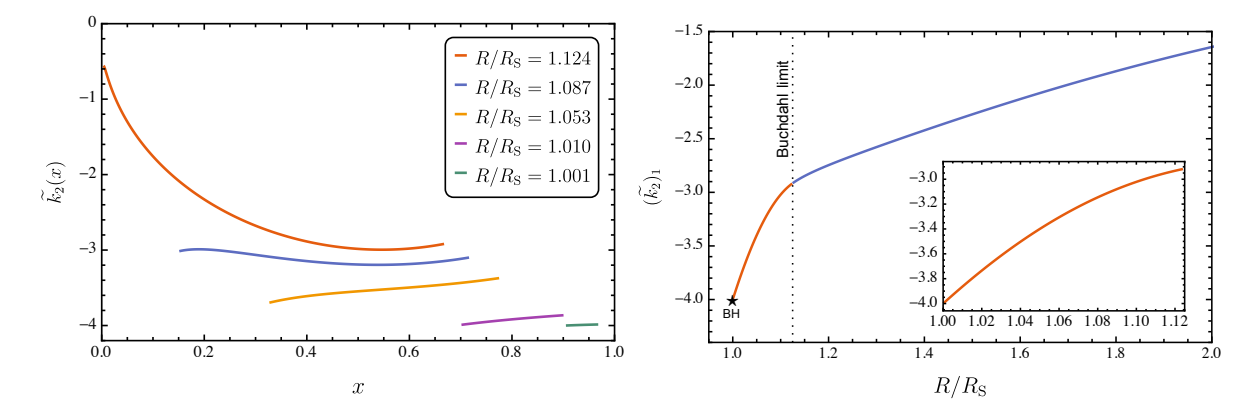


Figure 14. Left panel: Radial profile of the perturbation function $\widetilde{k_2}$, for various values of $R/R_{\rm S}$. **Right panel:** surface value $\widetilde{k_2}(1) = (\widetilde{k_2})_1$, as a function of the parameter $R/R_{\rm S}$. Observe that $(\widetilde{k_2})_1$ is finite and matches continuously at the Buchdahl limit; in the gravastar limit $R/R_{\rm S} \to 1$, $(\widetilde{k_2})_1 \to -4$.

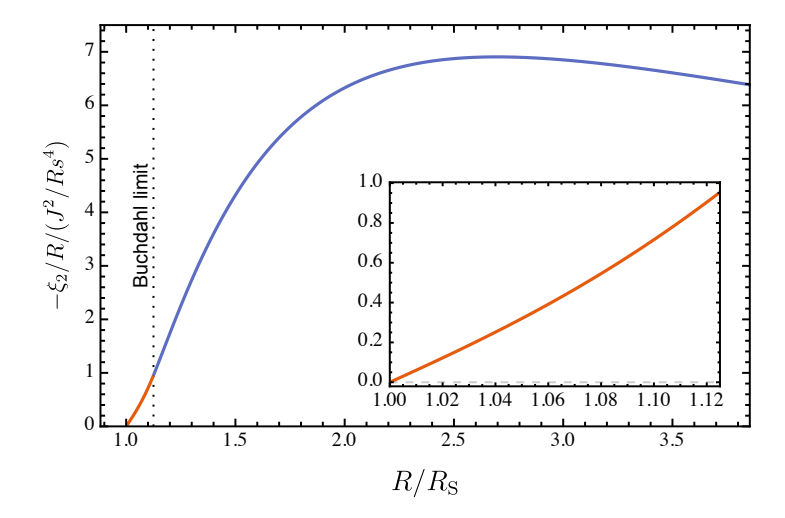


Figure 15. The function $-\xi_2(R)/R$, which determines the l=2 deformation of the boundary, as a function of the parameter $R/R_{\rm S}$. We measure $-\xi_2(R)/R$ in the unit $J^2/R_{\rm S}^4$.

corrects the value reported by [44]. In the gravastar limit $R/R_S \to 1$, we obtain

$$\varepsilon = \frac{6J^2}{R_{\rm S}^4}. ag{5.48}$$

Having determined all the perturbation functions for the slowly rotating Schwarzschild star in the gravastar limit, we proceed to determine the mass quadrupole moment Q, as given by (3.19). In figure 17 we show the 'Kerr factor' $\widetilde{Q} \equiv QM/J^2$, as a function of the parameter $R/R_{\rm S}$. This Kerr factor is relevant because it measures how much it deviates the exterior HT metric away from the Kerr metric ($\widetilde{Q} = 1$). We observe how \widetilde{Q} decreases monotonically as the compactness of the configuration increases. Our results for configurations above the Buchdahl limit, $R/R_{\rm S} > (9/8)$, are in very good agreement with those in [44]. However, at the Buchdahl limit we obtain $\widetilde{Q}(R_{\rm B}) = 1.0212$ which corrects the value reported by [44]. In the limit as $R \to R_{\rm S}$, we observe that \widetilde{Q}

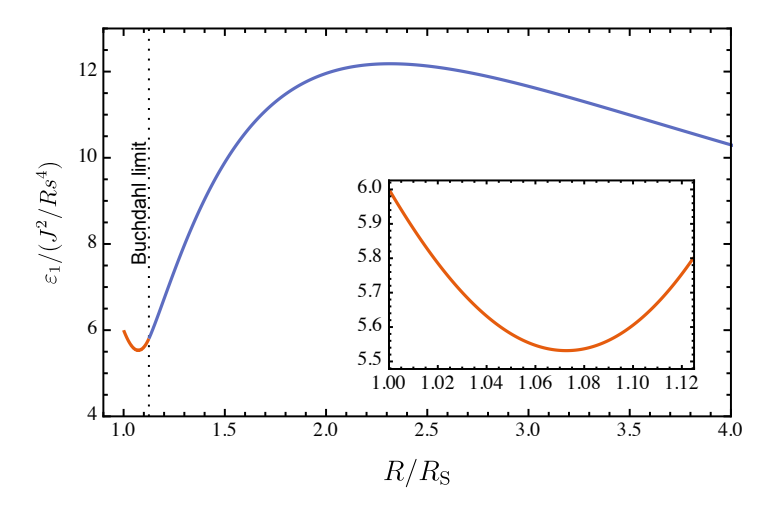


Figure 16. Ellipicity of the isobaric surfaces ε_1 , as a function of $R/R_{\rm S}$. In the gravastar limit $R \to R_{\rm S}$, $\varepsilon_1 = 6J^2/R_{\rm S}^4$.

approaches quickly to 1. Thus, we obtain that in the gravastar limit

$$Q = \frac{J^2}{M},\tag{5.49}$$

which agrees with the Kerr metric, within the approximation. Thus, we conclude that it is not possible to differentiate a slowly rotating Schwarzschild star, in the gravastar limit, from a Kerr BH, at the second-order in the angular velocity Ω . Finally, from

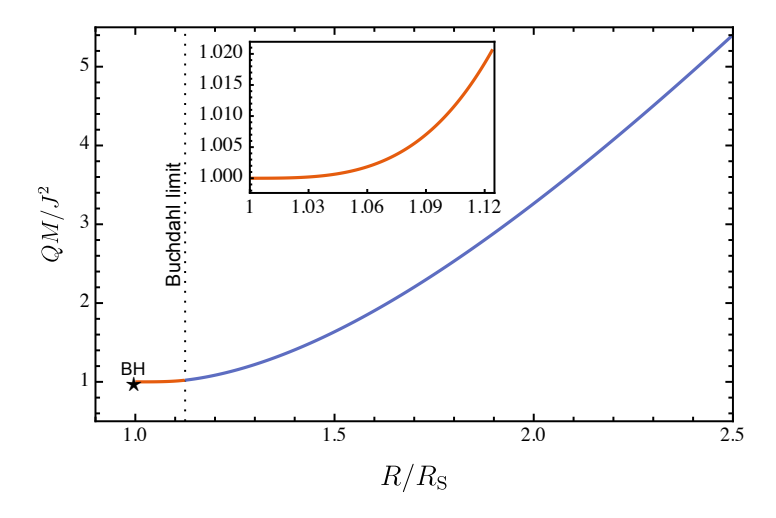


Figure 17. Kerr factor $\widetilde{Q} = QM/J^2$, as a function of the parameter $R/R_{\rm S}$. The inset zooms into the regime beyond the Buchdahl limit. Observe the smooth and continuous approach of \widetilde{Q} to the Kerr BH value, as $R \to R_{\rm S}$.

the results presented in figures 4 and 17, in figure 18 we display the $\bar{I}-\widetilde{Q}$ relation for slowly rotating Schwarzschild stars (dashed black curve). In the same figure, we also plot the universal fit of the $\bar{I}-\widetilde{Q}$ relations for realistic neutron stars (NSs) proposed by Yagi and Yunes (YY) [54] which is given as follows

$$\ln \bar{I} = a + b \ln(\tilde{Q}) + c(\ln \tilde{Q})^2 + d(\ln \tilde{Q})^3 + e(\ln \tilde{Q})^4, \tag{5.50}$$

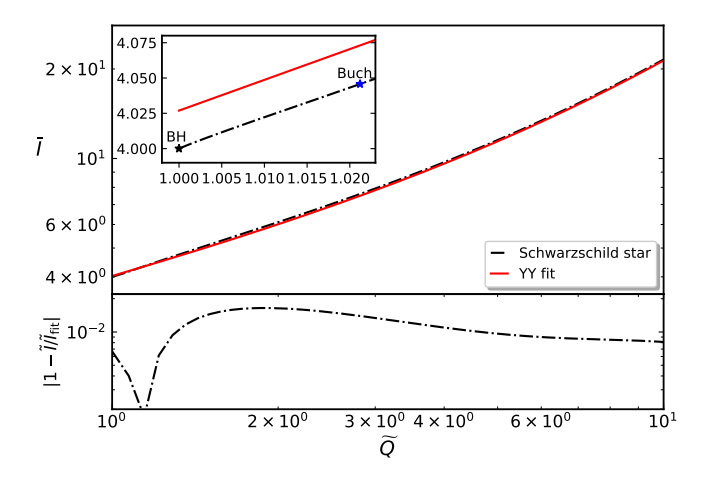


Figure 18. $\bar{I} - \widetilde{Q}$ relation for the Schwarzschild stars below and beyond the Buchdahl limit (dashed black curve). We include the analytic fitting formula (5.50) proposed by Yagi and Yunes [54] for realistic NSs (solid red curve). The inset zooms into the regime beyond the Buchdahl limit. The blue star indicates the Buchdahl bound, and the black star indicates the BH limit. In the bottom panel we show the fractional difference between the numerical results and the universal fit.

where the fitting coefficients are: a = 1.393, b = 0.5471, c = 0.03028, d = 0.01926 and $e = 4.434 \times 10^{-4}$. In the inset we enhance the region beyond the Buchdahl limit. Note that the $\bar{I} - \tilde{Q}$ relation for Schwarzschild stars approach exactly to the BH limit as $R \to R_{\rm S}$. We observe that deviations of the $\bar{I} - \tilde{Q}$ relation for the Schwarzschild stars, with respect to the universal YY fit, are $\mathcal{O}(1)\%$. While [52] considered the polytrope n = 0 (corresponding to an incompressible fluid with constant density) this shows that the fit is still reasonably accurate for Schwarzschild stars beyond the Buchdahl limit, despite the fact that the equations of state used to derive the fit in the first place are for lower density objects.

5.3.1. Inward extension of the quadrupole functions For the inward extension, $\varpi = 0$ everywhere inside the infinite pressure surface x_0 is uniquely well behaved, as such the behavior of the functions h_2 and v_2 , inside x_0 , becomes entirely dictated by the homogeneous equations (5.33), (5.34), while the behavior near x_0 is still specified by (5.35), (5.36). It is important to realize that for the homogeneous solution, $h_2^{(h)} \to 0$ on x_0 . Since in the region $0 < x < x_0$ we only have the homogeneous solution, we are forced to accept

$$h_2(x \to -\kappa^-) = 0. \tag{5.51}$$

In practice we do not have $h_2(x \to -\kappa^+) = 0$ for general cases (see left-hand panel of figure 12), which implies h_2 may be discontinuous at the infinite pressure surface. Once again, a finite discontinuity of an h perturbation function on x_0 is not a concern for g_{tt} overall because $e^{2\nu} \to 0$ there. However, we must have a continuous $k_2 = v_2 - h_2$ for

continuous $g_{\theta\theta}$. The structure of (5.35) and (5.36), together with the continuity of k_2 gives for the interior solution

$$C = \lim_{x \to -\kappa^+} (k_2). \tag{5.52}$$

Since k_2 typically does not go to zero as x_0 is approached from the outside (see left-hand panel of figure 14) the quadrupole functions must have a nonzero behavior in the region $0 < x < x_0$, unlike the monopole functions.

Unfortunately, inward integration of the quadrupole functions, given the boundary condition (5.52), typically leads to divergences at the origin. It is especially noteworthy that the behavior, as we approach the origin numerically (see figure 19), is

$$h_2, k_2 \propto x^{-3/2}$$
 (5.53)

which is equivalent to the r^{-3} behavior at the origin for the analytic k_2 and h_2 terms derived in [45].

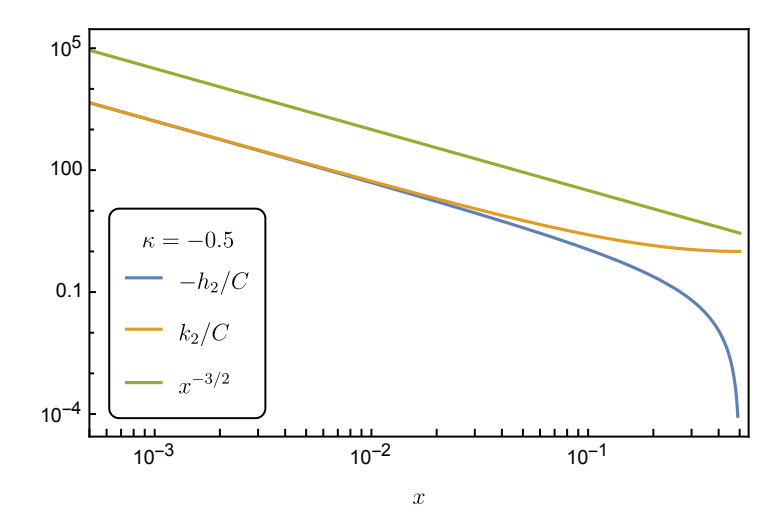


Figure 19. Log-Log plot of inward integration for k_2 and k_2 with asymptotic behavior highlighted for the example case of $\kappa = -0.5$. The function k_2 must be continuous across the infinite pressure surface and is generally nonzero, its value becoming the constant C for the homogeneous solution. The function k_2 goes to zero as we approach the infinite pressure surface from the inside. Both functions have $x^{-3/2}$ divergences at the origin.

6. Conclusions

In this paper we have reconsidered the problem of a slowly rotating homogeneous star, or Schwarzschild star, when its compactness goes beyond the Buchdahl limit and approaches the gravastar limit $R \to R_S$. For that purpose, we have employed the Hartle-Thorne (HT) framework for slowly rotating relativistic masses, at second order in the angular velocity Ω . In our approach, we contracted adiabatically, in a quasi-stationary process, a Schwarzschild star by taking its compactness beyond the Buchdahl limit. By

doing this process, we determined surface and integral properties associated to the region with positive pressure $x_0 < x < x_1$. In the gravastar limit as $R \to R_S$, $x_0 \to x_1$, thus this positive pressure region becomes essentially a boundary layer where the pressure is positive. Therefore, all the rotational properties of the configuration are associated with this boundary layer, while the interior de Sitter with negative pressure does not carry any angular momentum.

By imposing boundary conditions at the infinite pressure surface x_0 , rather than the origin, we were able to integrate the perturbation functions in the the corresponding region $x_0 < x < x_1$. The most important result of our study is that, in the gravastar limit, the perturbations and consequently quantities like the moment of inertia, and mass quadrupole moment, approach the corresponding Kerr metric values. Thus, within this approximation, it is not possible to differentiate a slowly rotating gravastar from a Kerr BH, by any measurements or observations in the exterior spacetime. Although we reached the same conclusions in [41], this study improves the one there where the study of the boundary conditions at x_0 was overlooked. However, in the relevant limit as $R \to R_S$, the results are in agreement.

Our approach is different from the one presented by [45], where the authors considered a gravastar fully formed, and they computed the perturbations in the interior de Sitter with negative pressure. Considering that the HT equations, as formulated here, cannot be applied to the interior $p = -\epsilon$, the authors derived the corresponding structure equations ab initio. We found that in the relevant limit when $R \to R_{\rm S}$ our results are in agreement with those in [45]. Extension of the perturbation functions into the negative pressure region $0 < x < x_0$, seems to lead to, in a best case scenario, divergences in the quadrupole perturbation functions at the origin. Interestingly, these divergences have qualitatively the same behavior $x^{-3/2} \propto r^{-3}$ as the corresponding quadrupole divergences at the origin found for the slowly rotating gravastar considered by [45].

One avenue for future investigation, would be to consider other sub-Buchdahl systems in slow rotation and see how they compare to our model. In particular, while perfect fluid spheres with positive pressure are limited by the Buchdahl bound, spheres with anisotropic stress can be more compact [55, 56, 57]. Although the original HT approximation deals with perfect fluids, extensions of the HT method which allow for treatment of anisotropic stress have recently been pioneered by [58, 59], therefore such a calculation may be possible.

7. Acknowledgements

P.B. would like to acknowledge Paolo Gondolo for partnership in work regarding series solutions for ϖ and divergences in m_0 in an unpublished project predating this one [47]. We would also like to thank Cecilia Chirenti, Paolo Gondolo and Emil Mottola for valuable discussions. C.P. acknowledges the support of the Institute of Physics and its Research Centre for Theoretical Physics and Astrophysics, at the Silesian University in

Opava.

Appendix A. Series solution to the dragging equation

Here we summarize the series solutions from (4.8) discussed by [47]. For that purpose, we introduce the new variable $z \equiv \kappa + x$ such that (4.8) takes the general form

$$A(z)\varpi(z)'' + B(z)\varpi(z)' + C(z)\varpi(z) = 0, (A.1)$$

where

$$A(z) = z(z - \kappa)(2 + \kappa - z), \tag{A.2}$$

$$B(z) = \kappa(2+\kappa) + 3(1+\kappa)z - 4z^2,$$
(A.3)

$$C(z) = -4(1+\kappa). \tag{A.4}$$

Let us investigate the regular singular point z=0. We can find a solution in terms of a Frobenius series as follows

$$\varpi_1(z) = z^2 \sum_{n=0}^{\infty} a_n z^n, \tag{A.5}$$

where the first few coefficients read

$$a_0 = 1, \quad a_1 = \frac{2(1+\kappa)}{\kappa(2+\kappa)}, \quad a_2 = \frac{17+24\kappa+12\kappa^2}{4\kappa^2(2+\kappa)^2}.$$
 (A.6)

The coefficients obey a recurrence relation of the form

$$i(i+2)\kappa(2+\kappa)a_i - (2i^2 + 5i - 1)(1+\kappa)a_{i-1} + i(i+3)a_{i-2} = 0.$$
 (A.7)

A second solution of ϖ can be obtained in the form

$$\varpi_2(z) = \sum_{n=0}^{\infty} b_n z^n - \frac{(1+\kappa)^2}{[\kappa(2+\kappa)]^2} \log(z^2) \varpi_1(z),$$
(A.8)

where the first few b coefficients are

$$b_0 = 1, \quad b_1 = \frac{4(1+\kappa)}{\kappa(2+\kappa)}, \quad b_2 = 0,$$

$$b_3 = -\frac{2(9\kappa^3 + 27\kappa^2 + 19\kappa + 1)}{3\kappa^3(\kappa + 2)^3}.$$
(A.9)

The recurrence relation for these coefficients is

$$-\frac{2(4i+13)(k+1)^{3}a_{i+1}}{k^{2}(k+2)^{2}} + \frac{2(2i+7)(k+1)^{2}a_{i}}{k^{2}(k+2)^{2}} + \frac{4(i+3)(k+1)^{2}a_{i+2}}{k(k+2)} + (i(2i+13)+17)(k+1)b_{i+3}$$

$$= (i+2)(i+5)b_{i+2} + (i+2)(i+4)k(k+2)b_{i+4}. \tag{A.10}$$

The most general possible solution to (A.1) could then be written as

$$\varpi_G = C_1 \varpi_1 + C_2 \varpi_2. \tag{A.11}$$

Suppose we look at ϖ_G at the infinite pressure surface. The ϖ_1 branch (A.5) goes to 0 as z^2 . Although the other branch (A.8) contains a term with a singular log factor, it is

multiplied by the solution from the a branch which goes to 0 fast enough to eliminate that term as $z \to 0$, such that the highest order behavior is $\varpi_2 \to b_0 = 1$; therefore

$$\lim_{z \to 0} \varpi_G = C_2. \tag{A.12}$$

From (4.9) for m_0 we obtain

$$\frac{dm_0}{dx} = \frac{8C_2^2(-\kappa)^{3/2}(\kappa+1)^2(\kappa+2)^{3/2}}{3(\kappa+x)^3} + \mathcal{O}\left((x+\kappa)^{-2}\right),\tag{A.13}$$

which after integration will lead to a divergent $(x + k)^{-2}$ term [47] that can only be cancelled by setting $C_2 = 0$. We can see from 5.9 that m_0 remains finite at $x = -\kappa$ if we use only the ϖ_1 branch. Therefore, unless it is explicitly stated otherwise, we use

$$\varpi = \varpi_1. \tag{A.14}$$

Appendix B. Consistency check

As mentioned previously in the paper, we have additional codes which compute quantities both in the (x, κ) coordinates and in the (r, R) coordinates. Here we examine the relative error defined by

$$e(Z) \equiv \left| \frac{Z_{x\kappa} - Z_{rR}}{Z_{x\kappa}} \right| ,$$
 (B.1)

where Z is some quantity computed in the indicated coordinates. We compute the error of various quantities for 600 evenly spaced points between $R/R_S = 1$ and $R/R_S = 4$.

For the first order frame dragging effects we examine $\widetilde{\Omega}$ and ϖ_1 . The average error in $\widetilde{\Omega}$ was 1.075×10^{-7} , the maximum was 2.19×10^{-7} at $R/R_{\rm S} = 3.7625$. The average error in ϖ_1 was 4.75×10^{-8} , the maximum was 2.82×10^{-6} at the lowest point tested $R/R_{\rm S} = 1.0025$ when $\varpi_1 \to 0$, which inflates the relative error as defined by (B.1).

For the monopole effects, we look at ξ_0/J^2 and δM . For δM , the average error is 5.34×10^{-6} and the maximum error is 1.48×10^{-4} which occurs at $R/R_{\rm S} = 1.0325$. For ξ_0/J^2 , the average error is 5.13×10^{-5} and the maximum error is 7.3×10^{-3} , at the lowest point tested $R/R_S = 1.0025$ when $\xi_0 \to 0$.

Finally, we can look at \widetilde{Q} and ξ_2/J^2 as examples for the quadrupole sector. For ξ_2/J^2 , the average error is 4.57×10^{-5} and the maximum error is 2.76×10^{-4} , at slightly above the Buchdahl limit $R/R_{\rm S}=1.1275$. For \widetilde{Q} , the average error is 6.87×10^{-5} and the maximum error is 4.24×10^{-4} at $R/R_{\rm S}=2.3075$.

Appendix C. Surface gravity parameter

In this appendix we discuss the surface gravity parameter for slowly rotating Schwarzschild stars. One convenient notation of the stationary axisymmetric metric in coordinates (t, r, θ, ϕ) is

$$ds^{2} = -e^{2\Phi}dt^{2} + e^{2\psi}(d\phi - \omega dt)^{2} + e^{2\alpha}dr^{2} + e^{2\beta}d\theta^{2}, \tag{C.1}$$

where Φ , ψ , α , β , and ω are functions of r and θ only. The functions Φ , ψ , and ω can be isolated as scalar functions due to the existence of the time and axial Killing vectors

$$K^{\mu}_{(t)} = (1, 0, 0, 0),$$
 (C.2)

$$K^{\mu}_{(\phi)} = (0, 0, 0, 1).$$
 (C.3)

We define additional vectors l and N, which in these coordinates are

$$l^{\mu} = (1, 0, 0, \omega), \tag{C.4}$$

$$N_{\mu} = (-1, -e^{\alpha - \Phi}, 0, 0), \tag{C.5}$$

such that

$$l = K_{(t)} + \omega K_{(\phi)}, \quad N \cdot N = 0, \quad N \cdot l = -1.$$
 (C.6)

With these auxiliary vectors, we can define two physically relevant scalar quantities, being the surface gravity parameter

$$S_G = N_\mu l_\nu (\nabla^\mu l^\nu) = \frac{1}{2} e^{-\alpha - \Phi} \frac{\partial}{\partial r} e^{2\Phi}, \tag{C.7}$$

and the angular momentum density parameter

$$\mathcal{J} = -N_{\mu} l_{\nu} (\nabla^{\mu} K^{\nu}_{(\phi)}) = -\frac{1}{2} e^{2\psi - \alpha - \Phi} \frac{\partial \omega}{\partial r}.$$
 (C.8)

These scalars are related to the Komar mass and angular momentum which can be defined as surface integrals at a given radius, or as the sum of a surface integral at a smaller radius and a volume integral of components of the energy-momentum tensor between the smaller and given radii [60, 61]

$$M_K(r) = \frac{1}{4\pi G} \int_{\partial V_+} (S_G + \omega \mathcal{J}) dA$$
 (C.9)

$$= \int_{V} \sqrt{-g} \left(-T^{t}_{t} + T^{r}_{r} + T^{\theta}_{\theta} + T^{\phi}_{\phi} \right) dr d\theta d\phi \tag{C.10}$$

$$+ \frac{1}{4\pi G} \int_{\partial V_{-}} (S_G + \omega \mathcal{J}) dA, \qquad (C.11)$$

$$J_K(r) = \frac{1}{8\pi} \int_{\partial V_+} \mathcal{J} \, dA \tag{C.12}$$

$$= \int_{V} \sqrt{-g} T^{t}_{\phi} dr d\theta d\phi + \frac{1}{8\pi} \int_{\partial V_{-}} \mathcal{J} dA.$$
 (C.13)

For his perturbative framework, Hartle [42] expanded the line element (C.1) in the form (3.1), with the following identifications

$$e^{\Phi} = e^{\nu(r)} \left[1 + h_0(r) + h_2(r) P_2(\cos \theta) \right],$$
 (C.14)

$$e^{\psi} = r \sin \theta \left[1 + k_2(r) P_2(\cos \theta) \right],$$
 (C.15)

$$e^{\alpha} = \left[1 + \frac{m_0 + m_2 P_2(\cos \theta)}{r - 2m}\right] \left(\frac{r}{r - 2m}\right)^{-1/2},$$
 (C.16)

$$e^{\beta} = r \left[1 + k_2(r) P_2(\cos \theta) \right],$$
 (C.17)

$$\omega = \omega(r), \tag{C.18}$$

where $\nu(r)$ corresponds to the nonrotating g_{tt} metric element. When expanded to second order, the parameters S_G and \mathcal{J} give

$$S_G = e^{\nu} \left[\nu' \left(1 + h_0 + h_2 P_2 - \frac{m_0 + m_2 P_2}{r - 2m(r)} \right)$$
 (C.19)

$$+h_0' + P_2(\cos\theta)h_2' \left[\left(\frac{r}{r - 2m(r)} \right)^{-1/2}, \right]$$
 (C.20)

$$\mathcal{J} = -\frac{r^2 \sin^2 \theta e^{-\nu}}{2\sqrt{\frac{r}{r-2m(r)}}} \omega'. \tag{C.21}$$

Appendix C.1. Surface gravity and angular momentum of Schwarzschild stars

For the nonrotating Schwarzschild star, $\mathcal{J} = 0$ and

$$S_G(\text{in}) = -\frac{Mr}{R^3} \operatorname{sgn}\left(\sqrt{1 - \frac{2Mr^2}{R^3}} - 3\sqrt{1 - \frac{2M}{R}}\right),$$
 (C.22)

$$S_G(\text{out}) = \frac{M}{r^2},\tag{C.23}$$

where $S_G(in)$ changes sign at the infinite pressure surface, due to the sign function. However, it is somewhat convenient to write everything in the x, κ variables such that

$$S_G(\text{in}) = \operatorname{sgn}(\kappa + x) \frac{\sqrt{x(2-x)}}{2\alpha}.$$
 (C.24)

For the slowly rotating Schwarzschild star, the functions S_G and $\mathcal J$ take the form

$$S_{G} = \frac{\sqrt{x(2-x)}}{2\alpha} \left[\operatorname{sgn}(\kappa + x) \left(1 + h_{0} + h_{2} P_{2} (\cos \theta) - \frac{m_{0} + m_{2} P_{2} (\cos \theta)}{\alpha (1-x)^{2} \sqrt{x(2-x)}} \right) + |x + \kappa| \left(h'_{0} + P_{2} (\cos \theta) h'_{2} \right) \right], \quad (C.25)$$

$$\mathcal{J} = -\frac{\alpha \left[x(2-x)\right]^{3/2} \sin^2 \theta}{|\kappa + x|} \omega',\tag{C.26}$$

where the prime now denotes derivative with respect to x. Inside the infinite pressure surface x_0 , we have

$$\varpi = 0, \quad h_0 = h_c(\text{in}),$$

 $m_0 = 0, \quad m_2, h_2 = O(x + \kappa)^2.$

Thus, taking the limit of (C.25) and (C.26), from below, i.e. $x \to -\kappa^-$, we get

$$S_G(x \to -\kappa^-) = -\frac{\sqrt{-\kappa(2+\kappa)}}{2\alpha} \left[1 + h_c(\text{in})\right], \qquad (C.27)$$

$$\mathcal{J} = 0. \tag{C.28}$$

As we approach x_0 from above, the perturbation functions take the behaviors

$$\varpi = \varpi_0(x+\kappa)^2, \quad h_0 = h_c(\text{out}),$$

$$h_2 = -\frac{4}{3} \left[\kappa(\kappa+2) \right]^3 (\alpha \varpi_0)^2.$$

The function m_2 can be found from h_2 and ϖ , but it is rather long so we do not write it down. Taking the limit from above, i.e. $x \to -k^+$, we obtain

$$S_G(x \to -\kappa^+) = \frac{\sqrt{-\kappa(2+\kappa)}}{2\alpha} \left[1 + h_c(\text{out}) \right], \tag{C.29}$$

$$\mathcal{J}(x \to -\kappa^+) = 2\alpha \left[-\kappa(\kappa + 2) \right]^{3/2} \varpi_0 \sin^2 \theta. \tag{C.30}$$

Note that there is a discontinuity in \mathcal{J} at the infinite pressure surface x_0 , which implies that there is a δ function in $\sqrt{-g}$ T^t_{ϕ} , so there is angular momentum density carried on x_0 . Likewise, there is also a δ function behavior in $\sqrt{-g}(T^{\mu}_{\mu})$ associated with the discontinuity in $S_G + \omega \mathcal{J}$. The discontinuity in \mathcal{J} is of the order Ω and the discontinuities in S_G and $S_G + \omega \mathcal{J}$, generally consist of order $\Omega^0 + \Omega^2$, although S_G may not have any Ω^2 discontinuity if $h_c(\text{in}) = -h_c(\text{out})$. On the other hand, if $h_c(\text{in}) = h_c(\text{out})$, then S_G has equal and opposite magnitude on each side of the surface which is the case for the nonrotating Schwarzschild star.

References

- [1] Hawking S W and Ellis G F R 1973 The Large Scale Structure of Space-Time (Cambridge: Cambridge University Press)
- [2] Penrose R 1965 Phys. Rev. Lett. 14 57–59
- [3] Hawking S W and Penrose R 1970 Proc. Roy. Soc. Lond. A 314 529-548
- [4] Wald R M 2001 Living Rev. Rel. 4 6
- [5] Chrusciel P T, Lopes Costa J and Heusler M 2012 Living Rev. Rel. 15 7
- [6] Barack L et al. 2019 Class. Quant. Grav. 36 143001
- [7] Abbott B P et al. (LIGO Scientific, Virgo) 2016 Phys. Rev. Lett. 116 061102
- [8] Abbott B P et al. (LIGO Scientific, Virgo) 2016 Phys. Rev. Lett. 116 241103
- [9] Akiyama K et al. (Event Horizon Telescope) 2019 Astrophys. J. Lett. 875 L1
- [10] Akiyama K et al. (Event Horizon Telescope) 2022 Astrophys. J. Lett. 930 L12
- [11] Hawking S W 1976 Phys. Rev. D 14 2460–2473
- [12] Chen P, Ong Y C and Yeom D 2015 Phys. Rept. 603 1–45
- [13] Chandrasekhar S 1983 The mathematical theory of black holes (Oxford: Oxford University Press)
- [14] Cardoso V and Pani P 2019 Living Rev. Rel. 22 4
- [15] Mazur P O and Mottola E 2023 Universe 9 88
- [16] Mazur P O and Mottola E 2004 Proc. Nat. Acad. Sci. 101 9545-9550
- [17] Visser M and Wiltshire D L 2004 Class. Quant. Grav. 21 1135–1152
- [18] Carter B M N 2005 Class. Quant. Grav. 22 4551–4562
- [19] Cattoen C, Faber T and Visser M 2005 Class. Quant. Grav. 22 4189–4202
- [20] DeBenedictis A et al. 2006 Class. Quant. Grav. 23 2303–2316
- [21] Lobo F S N and Arellano A V B 2007 Class. Quant. Grav. 24 1069–1088
- [22] Chirenti C B M H and Rezzolla L 2007 Class. Quant. Grav. 24 4191-4206
- [23] Pani P, Berti E, Cardoso V, Chen Y and Norte R 2009 Phys. Rev. D 80 124047
- [24] Pani P, Berti E, Cardoso V, Chen Y and Norte R 2010 Phys. Rev. D 81 084011
- [25] Cardoso V, Hopper S, Macedo C F B, Palenzuela C and Pani P 2016 Phys. Rev. D 94 084031
- [26] Chirenti C B M H and Rezzolla L 2008 Phys. Rev. D 78 084011
- [27] Cardoso V, Pani P, Cadoni M and Cavaglia M 2008 Phys. Rev. D 77 124044
- [28] Pani P 2015 Phys. Rev. D 92 124030 [Erratum: Phys.Rev.D 95, 049902 (2017)]
- [29] Uchikata N, Yoshida S and Pani P 2016 Phys. Rev. D 94 064015
- [30] Uchikata N and Yoshida S 2016 Class. Quant. Grav. 33 025005

- [31] Chirenti C and Rezzolla L 2016 Phys. Rev. D 94 084016
- [32] Rutkowski M and Rostworowski A 2021 Phys. Rev. D 104 084041
- [33] Das A, Ghosh S, Guha B K, Das S, Rahaman F and Ray S 2017 Phys. Rev. D 95 124011
- [34] Mazur P O and Mottola E 2015 Class. Quant. Grav. 32 215024
- [35] Schwarzschild K 1916 Sitzungsber. Preuss. Akad. Wiss. Berlin (Math. Phys.) 1916 424–434
- [36] Buchdahl H A 1959 Phys. Rev. 116 1027
- [37] Posada C and Chirenti C 2019 Class. Quant. Grav. 36 065004
- [38] Konoplya R A, Posada C, Stuchlík Z and Zhidenko A 2019 Phys. Rev. D 100 044027
- [39] Beltracchi P and Gondolo P 2019 Phys. Rev. D 99 084021
- [40] Chirenti C, Posada C and Guedes V 2020 Class. Quant. Grav. 37 195017
- [41] Posada C 2017 Mon. Not. R. Astron. Soc. 468 2128–2139
- [42] Hartle J B 1967 Astrophys. J. 150 1005–1029
- [43] Hartle J B and Thorne K S 1968 Astrophys. J. 153 807
- [44] Chandrasekhar S and Miller J C 1974 Mon. Not. R. Astron. Soc. 167 63–80
- [45] Beltracchi P, Gondolo P and Mottola E 2022 Phys. Rev. D 105 024002
- [46] Uchikata N and Yoshida S 2014 Phys. Rev. D 90 064042
- [47] Beltracchi P and Gondolo P 2021 Frame dragging of the sub-Buchdahl Schwarzschild star (unpublished)
- [48] Reina B 2016 Mon. Not. R. Astron. Soc. 455 4512–4517
- [49] Reina B and Vera R 2015 Class. Quant. Grav. 32 155008
- [50] Mars M 2005 Class. Quant. Grav. 22 3325–3348
- [51] Posada C and Stuchlík Z 2023 Class. Quant. Grav. 40 135009
- [52] Yagi K and Yunes N 2013 Phys. Rev. D 88 023009
- [53] Yagi K and Yunes N 2013 Science **341** 365–368
- [54] Yagi K and Yunes N 2017 Phys. Rept. 681 1–72
- [55] Bowers R L and Liang E P T 1974 Astrophys. J. 188 657–665
- [56] Lemaitre G 1997 Gen. Relativ. Gravit. 29 641–680
- [57] Ovalle J, Posada C and Stuchlík Z 2019 Class. Quant. Grav. 36 205010
- [58] Pattersons M L and Sulaksono A 2021 Eur. Phys. J. C 81 698
- [59] Beltracchi P 2022 Phys. Rev. D 106 104038
- [60] Komar A 1959 Phys. Rev. **113**(3) 934–936
- [61] Beltracchi P, Gondolo P and Mottola E 2022 Phys. Rev. D 105 024001